Modeling the Northern eddy-driven jet stream position and wind speed variability with stochastic coupled non-linear lattices

Robin Noyelle, Davide Faranda, Pascal Yiou

Modeling the Northern eddy-driven jet stream position and wind speed variability with stochastic coupled non-linear lattices

Robin Noyelle,[a] Davide Faranda,[a b c] Pascal Yiou,[a]

[a] *Laboratoire des Sciences du Climat et de l'Environnement, UMR 8212 CEA-CNRS-UVSQ, Université Paris-Saclay & IPSL, CE Saclay l'Orme des Merisiers, 91191 Gif-sur-Yvette, France*

[b] *London Mathematical Laboratory, 8 Margravine Gardens, London, W68RH, UK*

[c] *LMD/IPSL, Ecole Normale Superieure, PSL research University, Paris, France*

Corresponding author: Robin Noyelle, robin.noyelle@lsce.ipsl.fr

ABSTRACT: At the synoptic time scale, the northern mid-latitudes weather is dominated by the influence of the eddy-driven jet stream and its variability. The usually zonal jet can become mostly meridional during so-called blocking events, increasing the persistence of cyclonic and anticyclonic structures and therefore triggering extremes of temperature or precipitation. During those events, the jet shifts northerly or southerly with respect to its mean position. Previous research proposed theoretically derived 1D models of the jet stream to represent the dynamics of such events. Here, we take a data-driven approach using ERA5 reanalysis data over the period 1979-2019 to investigate the variability of the eddy-driven jet latitudinal position and wind speed variability. We show that shifts of the jet latitudinal position occur on a daily time scale and are preceded by a strong decrease of the jet zonal wind speed, 2-3 days prior to the shift. We also show that the dynamics of the zonal wind speed at the jet location can be modelled by a non-linear oscillator with stochastic perturbations. We combine those two results to propose a simple 1D model capable of representing the statistics and dynamics of blocking events of the eddy-driven jet stream. The model is based on two stochastic coupled non-linear lattices representing the jet latitudinal position and zonal wind speed. Our model is able to reproduce temporal and spatial characteristics of the jet. We highlight a potential link between the propagation of solitary waves along the jet and the occurrence of blocking events.

SIGNIFICANCE STATEMENT: The meanders of the atmospheric jet stream trigger extreme events in the mid-latitude regions, such as heat waves and cold spells. It is therefore of primary importance to better understand the variability of the jet position. This paper investigates this variability and shows that it can be modelled using coupled non-linear lattices. Our results suggest the possibility of using simple dynamical models to represent the complex dynamics of atmospheric features such as the jet stream.

1. Introduction

The northern mid-latitudes weather and its variability are dominated by the influence of strong zonal westerlies winds located around the tropopause, with a narrow latitudinal extension — a feature known as the jet stream (Charney 1947; Holton 1973; Hurrell and Deser 2010). There are actually two jets arising from two different physical mechanisms: the so-called "thermally-driven" jet (Held and Hou 1980) and the so-called "eddy-driven" jet (Held 1975; Rhines 1975). However, those two jets are not always distinguishable as they can be located around the same latitudes and therefore mix to create what is called a "merged" jet (Lee and Kim 2003; Messori et al. 2021).

The jet stream has a typical spatial and temporal variability of a few thousand kilometers and of 10 days. This variability is not well represented in most climate models for misunderstood reasons (Davini and d'Andrea 2020) and seems to be sensitive to the model resolution only in some regions (Davini and D'Andrea 2016; Attinger et al. 2019). This shortcoming is crucial as the jet can trigger extreme events in the mid latitudes (Kautz et al. 2021). One strategy to overcome this limitation is to propose an explicit but simplified formulation of the dynamics of the jet.

Even though the climatology of winds in the upper troposphere displays a mostly zonal flow, the jets can present large northward and southward meanders (e.g. Koch et al. 2006; Röthlisberger et al. 2016) on the synoptic timescales ($\approx$ 10 days). The flow can even become mostly meridional, or even split or break (Haines and Malanotte-Rizzoli 1991). Those meanders allow air masses coming from the south or the north to persist around mid-latitudes regions, potentially triggering temperature or precipitation extremes (e.g. Dole et al. 2011; Kautz et al. 2021, for a recent review). It is therefore of primary importance to better understand the dynamics of the jet meanders and how it will change with climate change (Woollings et al. 2018a).

The seminal paper of Charney and DeVore (1979) showed the existence of multiple flow equilibria in a simple barotropic channel model. This framed the dynamics of meanders and splits in terms of transitions between two situations: zonal, where the jet flows parallel to latitude lines, and blocked, where the jet makes large northward and southward excursions which can last several days and break the zonal symmetry — two situations already identified by Rex (1950).

Many explanations have been suggested for the existence of blocked situations in the atmosphere (Lupo 2020), from multiple equilibria in a barotropic flow (Charney and DeVore 1979; Legras and Ghil 1985; Ghil 1987) to resonant or quasi-resonant amplification of Rossby waves (Tung and Lindzen 1979; Mann et al. 2018) or barotropic/baroclinic instability (Simmons et al. 1983; Frederiksen 1982). Other theories have characterized blocking episodes as a manifestation of multiple equilibria in asymmetrically forced flows (Hansen 1986) or soliton-modon structures (McWilliams et al. 1981). Faranda et al. (2016) studied the hypothesis of blocking episodes as unstable fixed points of the atmospheric mid-latitude circulation in a reduced phase space constructed using circulation indices capable to track the symmetry of the mid-latitude flow.

Here we propose a data-driven 1D model of blocking events that is calibrated on reanalysis data. In this model, we represent the latitudinal position of the jet as a function of longitude only. We build on the work of Faranda et al. (2019) who also proposed a 1D minimal dynamical system to reproduce the characteristics of breaking events of the jet by an embedding of climate data, and Nakamura and Huang (2018) who proposed a 1D model of blocking events using an analogy with traffic jams. We propose a similar approach but focus on the onset and decay of blocking events. Our model is based on the coupling between the zonal wind speed on the jet and the latitudinal position of the jet itself. We also present analyses of the spatio-temporal behavior of the proposed model and comparisons with reanalysis data.

This paper is organized as follows: in section 2, we detail the data used and the methods and tools from dynamical system theory that we will be applying. In section 3 we provide the result of the investigations led on the data and present a point model to represent blocking events. Section 4 presents the proposed 1D model and assesses its results with regards to reanalysis data. Finally, the discussion of the results is led in 5 and conclusions are drawn in section 6.

2. Data and methods

a. Data and jet position algorithm

The analysis and the model proposed here are based on the ERA5 reanalysis data of the European Centre for Medium Range Weather Forecasts (Hersbach et al. 2020). We use daily average data with a 0.25° horizontal resolution over the 1979–2019 period for the Northern Hemisphere between 15°N and 75°N. The variables considered are the geopotential height at 500hPa (mid-troposphere) and horizontal wind speed between 850 and 700hPa.

The method used to diagnose the jet position is close to the ones proposed by Woollings et al. (2010) and Faranda et al. (2019). The former employed wind speed averaged over 925–700hPa pressure levels (low-level jet), whereas the latter considered the average over 200–400hPa (high-level jet).

The two jets (thermally-driven (Held and Hou 1980) and eddy-driven (Held 1975; Rhines 1975)) behave differently across the troposphere: the subtropical jet is located on the upper troposphere and displays a strong vertical shear, whereas the eddy-driven jet has a barotropic structure extending to almost all the troposphere (Woollings et al. 2010). To avoid mixing the two jets in the diagnosis of the jet position, we chose to take daily mean wind speed averaged over 850–700hPa pressure levels as the eddy-driven jet is only detectable within these pressure heights. We therefore assume that the barotropic nature of this eddy-driven jet for the position of the jet is well diagnosed. We also apply a 10 days low-pass Lanczos filter to remove the influence of transient eddies (Duchon 1979) as in Woollings et al. (2010).

To find the position of the jet at each day, we use a two-step algorithm. The first step consists in finding, for each longitude, the latitude at which the wind horizontal kinetic energy $E = \frac{1}{2}\vec{u}_H^2$ is maximum. The second step is to apply a 25° rolling median to the previous positions found. This rolling median is applied to avoid a nonphysical detection of breaks in the jet, as with a 0.25° horizontal resolution and considering the low-level jet, the algorithm sometimes detects high-wind speeds in the lee of mountains. This is especially the case in the Atlantic region around Greenland. 25° approximately corresponds to 2000km at 45°N, which is also the typical size of mid-latitudes baroclinic disturbances (Hoskins and James 2014) so that this rolling median has a physical basis. Finally, once we have the position of the jet diagnosed by this algorithm, we also consider the zonal

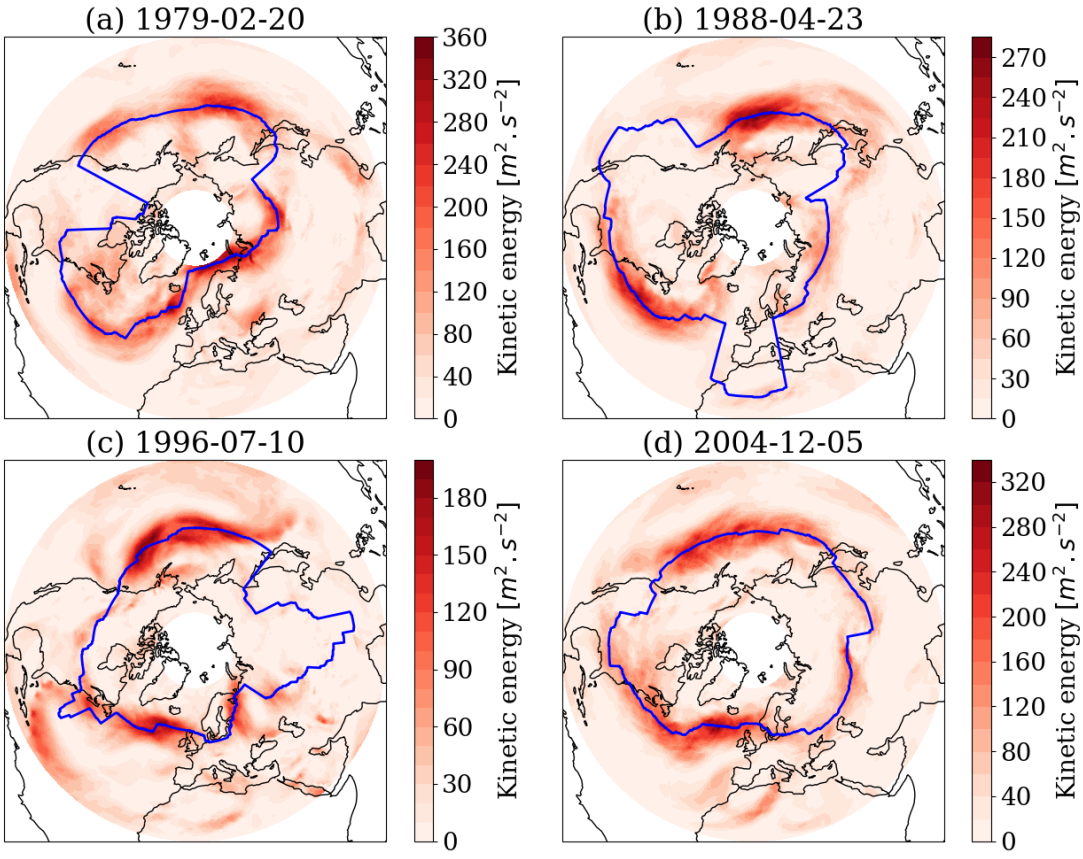

FIG. 1. **Horizontal wind kinetic energy and jet position**. Snapshots of horizontal wind kinetic energies E (colors) and jet positions determined by the algorithm (blue line) from ERA5 data for four dates in the 1979-2019 period: (a) 20th February 1979, (b) 23rd April 1988, (c) 10th July 1997 and (d) 5th December 2004).

and meridional wind speed on the jet as being the values of zonal and meridional wind speed at the latitudes found for the jet position by the algorithm.

Figure 1 shows snapshots of the horizontal wind kinetic energies and jet positions determined by the algorithm for four arbitrary dates in the period studied (20th February 1979, 23rd April 1988, 10th July 1997 and 5th December 2004). The four dates illustrate the behavior of the jet for the four seasons and as one can notice, the jet is much stronger and well defined during the winter season, which is consistent with Woollings et al. (2010). As a consequence, in the following — especially for the model design — we will focus on the winter behavior of the eddy-driven jet.

b. Local dynamical systems metrics

The dynamical relevance of the proposed model will be assessed matching some important dynamical quantities of the model with those extracted from the data. As the atmospheric dynamics can be formulated in terms of a complex dynamical system (Ghil et al. 2008; Dijkstra 2016; Ghil and Lucarini 2020), it is natural to investigate the properties of its attractor.

We will use dynamical systems metrics: the local dimension of the attractor d and the persistence of phase-space trajectories θ^{-1}, which both characterise instantaneous state of a system in the phase-space (Lucarini et al. 2016; Faranda et al. 2017). Both of these metrics are computed using the fact that the probability for a recurrence of a system configuration (a state) can be linked to the generalized Pareto distribution. To compute this probability from data, we compute the series of distances $\mathrm{dist}(x(t), \zeta)$ between a state of the system ζ and all other points $x(t)$ on the trajectory of the system. This time series of distances is then transformed into: $g(t) = -\log(\mathrm{dist}(x(t), \zeta))$ so that being close to state ζ is equivalent to exceeding a threshold $s(q)$ where q is a percentile of the series $g(x(t))$. We will use the 97.5% percentile of all values of $g(t)$, which ensures to have enough data while keeping only the extremes. It can be shown that the probability distribution of $g(t)$ when it exceeds $s(q)$ converges to a Pareto distribution (Lucarini et al. 2016) with scale parameter σ, and a shape parameter $\xi = 0$.

The local dimension d is defined as the inverse of the scale parameter of the generalized Pareto distribution fitted on the data which satisfies $g(x(t)) > s(q)$. d is a proxy for the system's active number of degrees of freedom when reaching a region of phase space, so that even when considering a system with a large number — possibly infinite — of degrees of freedom, d provides the local number of dimensions that the system can be summarized to. Therefore a state 1 with a local dimension d_1 greater than the local dimension $d_2 < d_1$ of another state 2 means that the behavior of the system around state 1 has more dimensions on which to evolve and is therefore less predictable than around state 2. Additionally, Pons et al. (2020) showed that d can be used as a measure of synchronization: a low value of d is associated with a high degree of synchronization between the variables defining the system.

The second dynamical system metrics that we will be using is the persistence θ^{-1} of a given state ζ on the attractor, which is equivalent to the mean residence time of the trajectories when they enter the neighborhood of ζ. This metric corresponds to a well defined statistical quantity introduced

in extreme value statistics, namely the extremal index θ. The latter is here estimated using the Süveges (2007) estimator. Note that in the framework of dynamical systems, we find $\theta = 0$ at stable fixed points of the dynamics (the trajectory resides an infinite amount of time in the neighborhood of this state), with an infinite number of infinitely time resolved trajectories. Instead, $\theta = 1$ is found at non persistent states of the dynamics (see Moloney et al. (2019) for more details). In general, for time-continuous systems sampled at a given resolution dt, $\theta^{-1} > 1$. For daily sea-level pressure fields over the North Atlantic, Faranda et al. (2017) found θ^{-1} values varying between 2 and 3 days ($0.3 < \theta < 0.5$).

c. Blocking metrics

In order to objectively diagnose blocking events we use the classical blocking index of Tibaldi and Molteni (1990) defined as follows. For each longitude, two geopotential height gradients are computed:

$$\begin{cases} GHGS = \frac{Z(\phi_0) - Z(\phi_s)}{\phi_0 - \phi_s}, \\ GHGN = \frac{Z(\phi_n) - Z(\phi_0)}{\phi_n - \phi_0} \end{cases} \tag{1}$$

where:

$$\begin{cases} \phi_n = 80°N + \Delta, \\ \phi_0 = 60°N + \Delta, \\ \phi_s = 40°N + \Delta, \\ \Delta = -4°, 0° \text{ or } 4°. \end{cases}$$

A given longitude is said to be "blocked" at a specific instant in time if for at least one value of Δ:

1. $GHGS > 0$,
2. $GHGN < -10 m/°lat$.

Using this index, "blocking" is an instantaneous and local property of each longitude. However, blocking events usually have a large spatial and temporal extension. Therefore, we follow Tibaldi and Molteni (1990) by defining for each longitude (i) large scale blocking if longitudes are blocked within a range of 15° around this longitude and (ii) episodes blocking if longitudes are blocked within a range of 10° for at least 4 days. The smaller spatial extent used for episodes blocking allow blocked longitudes to slightly move.

There is no unique way to define blocking, and therefore many diagnostics tools are available in the literature (Schwierz et al. 2004; Pelly and Hoskins 2003; Barriopedro et al. 2010) — especially 2D blocking indices (Scherrer et al. 2006; Masato et al. 2013). Here we choose to use the Tibaldi and Molteni (1990) index because it is a widely used index in the literature, its definition is simple and more importantly it is a 1D index. In the following we use this index for illustration and checking purposes and our analysis is not based on the relevance of this index. Therefore, the choice of one index over another should not have a great impact.

3. Jet behavior and construction of the model

In this section, we display results on the dynamical characteristics of the eddy-driven jet stream and we propose a stochastic point model of the onset and decay of blocking events on the jet. As mentioned earlier, the eddy-driven jet stream is much stronger — and hence well-defined — in winter than during the other seasons. Therefore, even though we will show empirical behavior of the jet during each season, the model will be built by solely restricting the data set to winter months (December to February).

a. Climatology of jet positions, blocking events and dynamic metrics

First, Figure 2 displays the climatology of jet positions found with our algorithm, namely the probability density of latitudes where the jet is located for each longitude, splits into the four seasons. The densities presented in the figure are consistent with previous climatologies of the jet position in terms of mean latitudes (Woollings et al. 2018b), except for summer where for some longitudes mainly in Asia the algorithm seems to track the subtropical jet at the southern part of the spatial domain under study for some longitudes. If we focus on the winter season, we see that the jet is located in a very narrow band of latitude at the west of the ocean basins (North Atlantic and

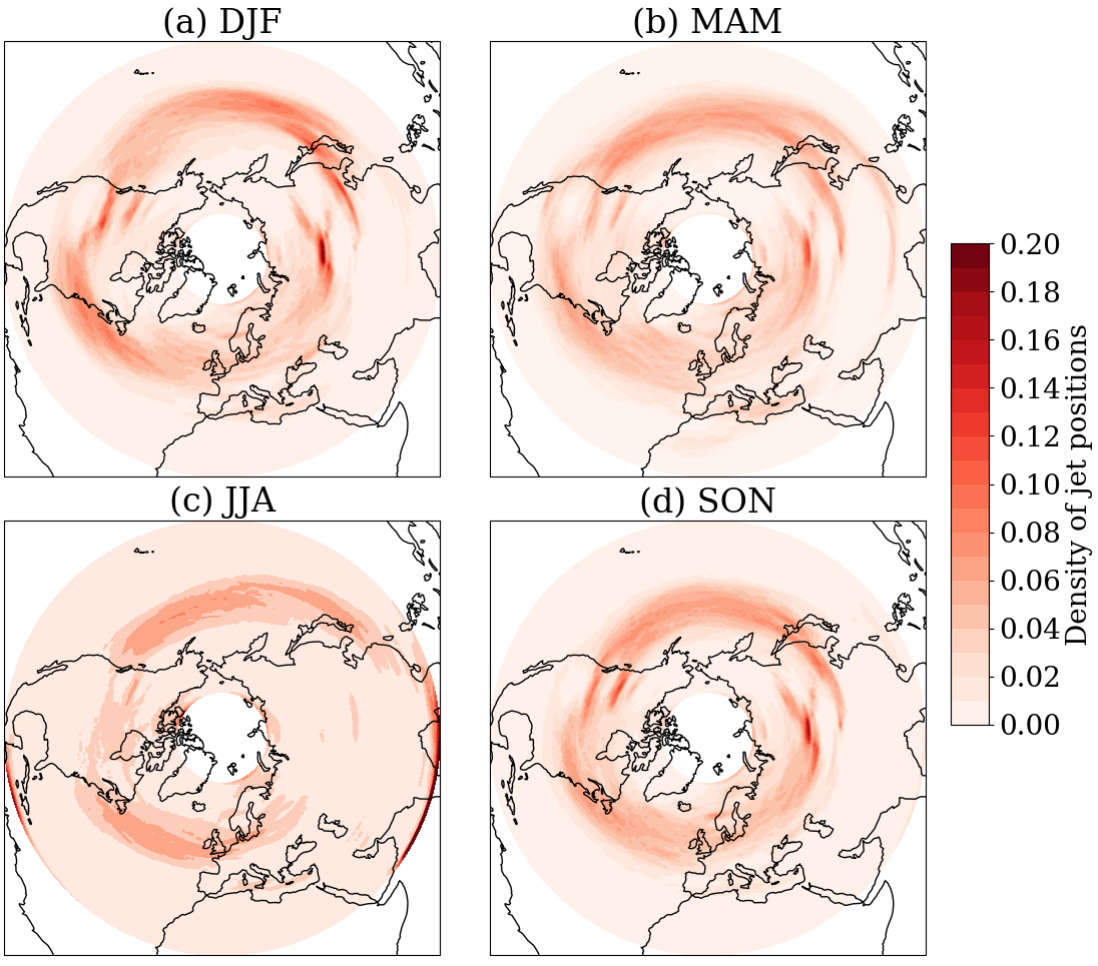

FIG. 2. **Probability density of the jet positions for the four seasons over the period 1979-2019.**

North Pacific) whereas the spread is much more important at the east of those basins. As we will show (see in particular Figure 3), those locations are the preferential places where blocking events occur. One drawback of using low level jet is that its position is not well detected over mountain ranges. Indeed, the jet over the Rocky mountains is located in a very narrow latitudinal band in Figure 2.

Figure 3 displays the frequency of blocking for each longitude for each season. We use the three Tibaldi and Molteni (1990) indicators defined above: local blocking (plain lines), large scale blocking (dotted line) and episodes blocking (dashed lines). As one could expect, local blocking is more frequent than large scale blocking, the latter being more frequent than episodes blocking. Blocking frequencies vary strongly from season to season and from longitudes to longitudes, ranging from almost 0% at 100°W in summer to almost 20% at 0° in spring, which is consistent

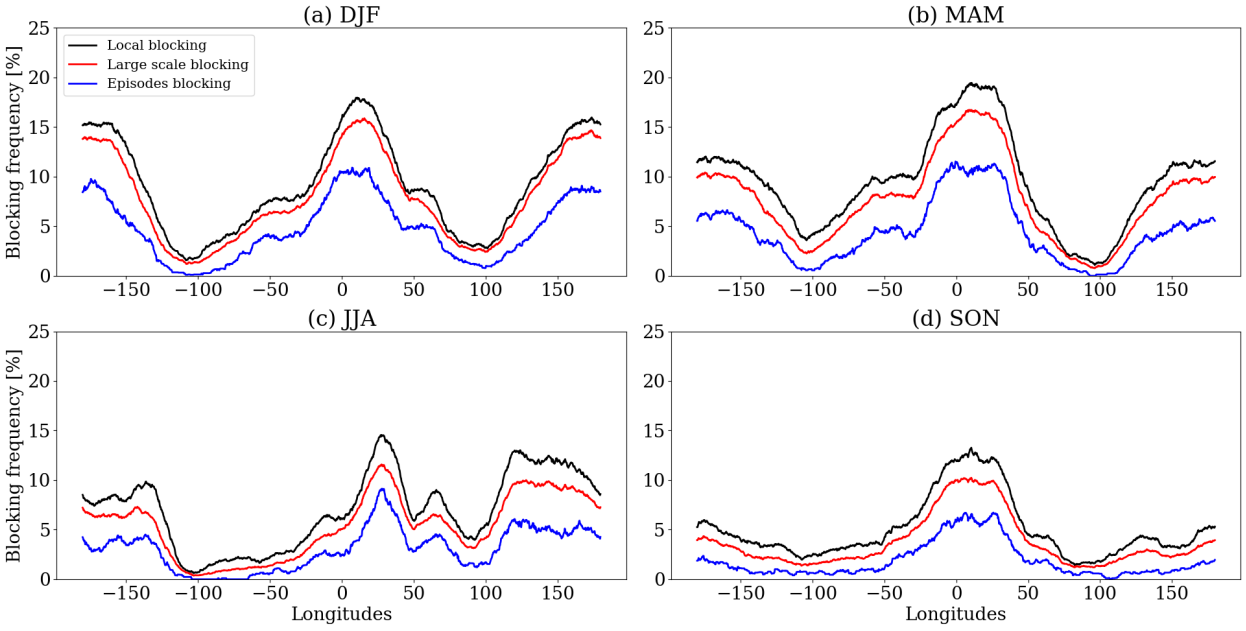

FIG. 3. **Blocking frequencies for each longitudes for the four seasons (1979-2019).** We display the three indexes defined in c: local blocking (black), large scale blocking (red) and episodes blocking (blue).

with the literature (Barriopedro et al. 2006; Tyrlis and Hoskins 2008; Lupo 2020). For winter, the longitudes which are the most often blocked are located near 0° and near 180°W, which are longitudes closed to the one with the maximum spread of jet positions.

Figure 4 shows the analysis made on the series of the jet positions using the dynamic metrics defined in section 2b. Figure 4 panel (a) displays the histograms of local dimension and local persistence for the jet. It should be emphasized that those metrics are computed on the vectors of the latitudinal positions of the jet, which, as the horizontal resolution is 0.25°, cover all the Northern hemisphere and have a length of 1440 grid points. Therefore, finding local dimensions, i.e. approximately the number of degrees of freedom, between 5 and 20 suggests that this dynamics is rather low dimensional. This is consistent with the results found in Faranda et al. (2017) who used SLP data for a similar analysis. Figure 4 panel (b) shows the evolution of the two metrics over the entire period with a one year rolling median (red and blue curves) and a 10 year rolling median (corresponding black curves). As one can see, there are strong inter-annual variations, and even inter-decadal variations as for example there is a clear decreasing trend of the local dimension

between 1980 and 2005 (from $d \approx 12$ to $d \approx 11.5$) which is consistent with the variations in the jet variability identified by Woollings et al. (2018b).

Figure 4 panels (c) and (d) displays d-θ^{-1} plots of two measures of the jet non zonality: the percentage of latitudes that are blocked (using the large scale blocked index) and the waviness, which we define as the horizontal standard deviation. Apart from the overall negative correlation between d and θ^{-1} (states with a lot of degrees of freedom are less persistent), which has already been identified (e.g. Faranda et al. 2017), there does not seem to be any link between our two measures of non zonality and the two metrics. The reason could be that we are computing mutual distances between the positions of the jet over the entire Northern Hemisphere, therefore taking into account different disconnected weather regimes. In Figure 5 we provide the same analysis as in Figure 4 but we computed the mutual distances only over the Euro-Atlantic sector (45°W-45°E). Even though the percentage of large scale blocked longitudes does not show any structure, there is a clear structure in the waviness indicator: high waviness is correlated with a higher local dimension and a lower persistence, which is consistent with the hypothesis of Faranda et al. (2016) that blocking events, i.e. states with a high waviness, are fixed points of the dynamics (low persistence and high dimension).

b. Jet position and blocking events dynamics

We now investigate whether a 1D stochastic model of the jet can be used to represent the dynamics and statistics of blocking events. We wish to represent the jet latitudinal position as a function of longitude only and therefore we will investigate dynamical constraints for such a model. The first step is to investigate whether the jet position can be used as an effective tool for diagnosing blocking events. Figure 6 panel (a) shows the probability density of jet positions at longitude 0° in the case of blocked and non blocked situations for winter (1979-2019) using Tibaldi and Molteni (1990) large scale blocking index and Figure 6 panel (b) displays probability density difference of jet positions in the case of blocked and non blocked situations for all longitudes. In Figure 6 panel (b), red (resp. blue) regions indicate that the jet has a higher (resp. lower) probability to be at that latitude when it is blocked.

The behavior of the blocked jet in Fig. 6 is consistent with the switching between a zonal jet (mainly in blue) with a meandering jet (in red), the latter displaying large northward and southward

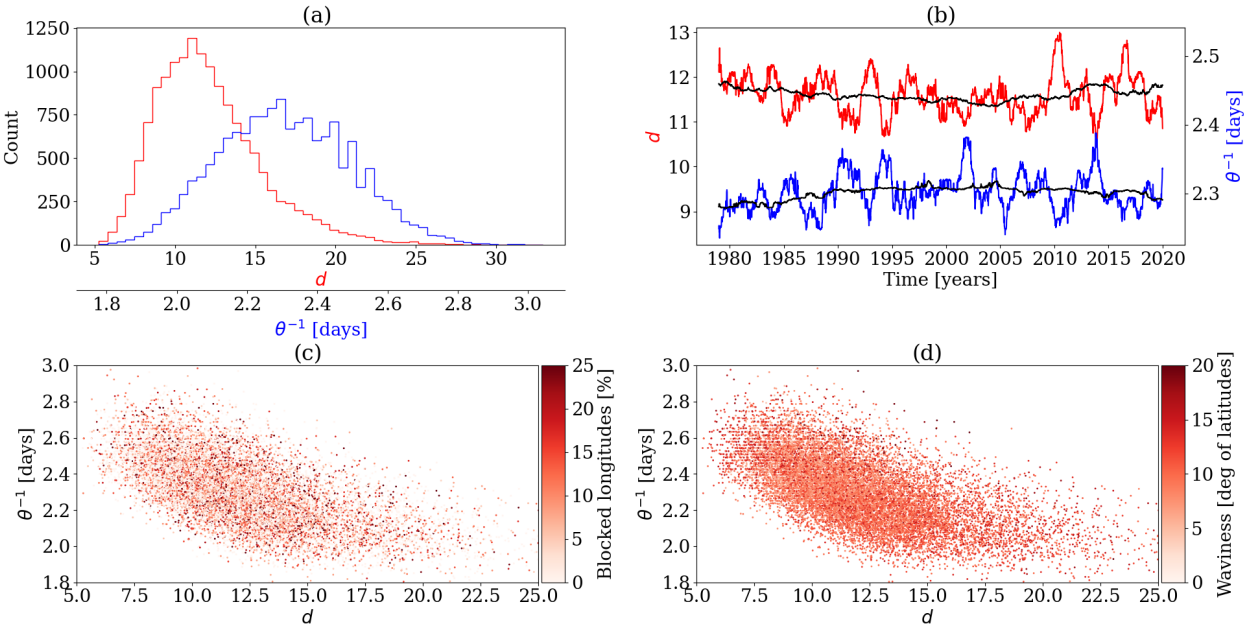

FIG. 4. **Analysis of the jet positions using local dynamical system metrics.** (a) Histograms [day counts] of local dimension d (red) and local persistence θ^{-1} (blue) of the jet positions over the entire Northern hemisphere. (b) one year rolling median for 1979-2019 time series of d (red) and θ^{-1} [days] (blue). Black curves indicate a ten years rolling median. (c) scatter-plot of d–θ^{-1} [days] computed on the Northern hemispheric jet positions. Colorscale indicates the percentage of large-scale blocked longitudes. (d) Same as in (c) with waviness (computed as the horizontal jet-position standard deviation) in colors.

excursions when it is diagnosed as blocked. One should note that, when using the blocking index of Tibaldi and Molteni (1990), the preferred jet position is different from one longitude to another: northward (resp. southward) in the east (resp. west) of the Atlantic basin. Figure 6 shows that blocking situations are associated with anomalous jet positions, either northward or southward. Thus the jet position can be used as an alternative index of a blocked situation, a point on which we will build our 1D model.

The analysis reported in Figure 6 is performed with 0.25° increments in longitude. If we consider the differences between jet position densities conditional on blocking at longitude 0° only and not blocked at each longitude, the structure close to 0° is very similar, i.e. with a large northward meander (not shown).

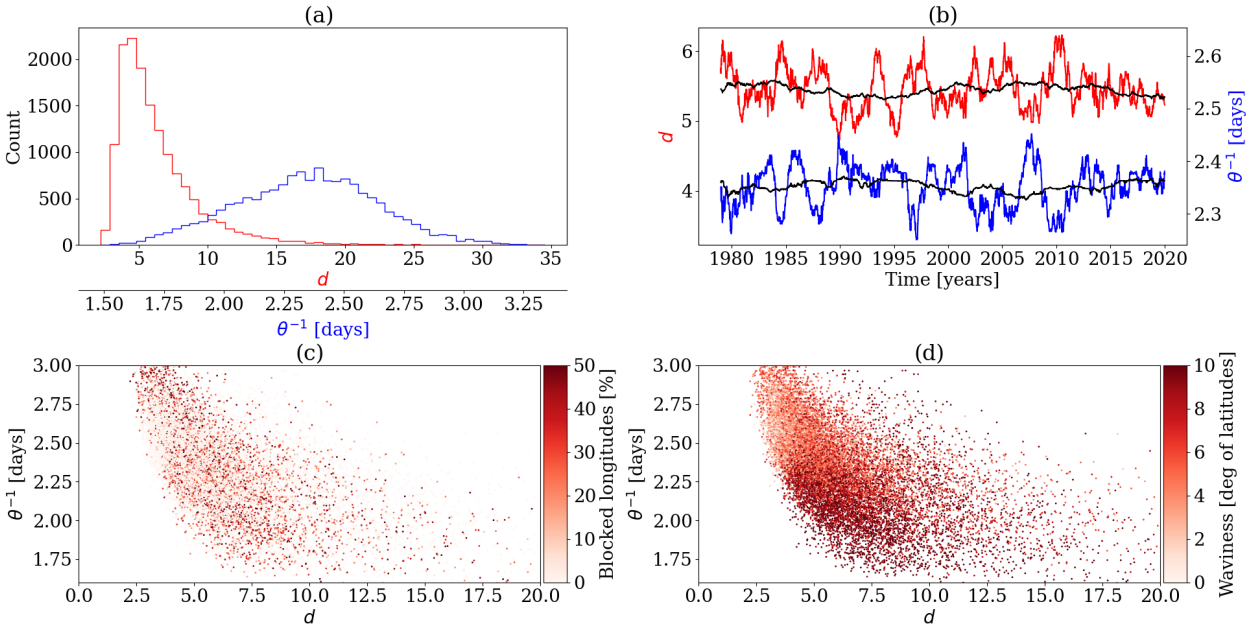

FIG. 5. **Analysis of the jet positions over the Euro-Atlantic sector using local dynamical system metrics.** (a) Histograms [day counts] of local dimension d (red) and local persistence θ^{-1} (blue) of the jet positions over the Euro-Atlantic sector (45°W-45°E). (b) one year rolling median for 1979-2019 time series of d (red) and θ^{-1} [days] (blue). Black curves indicate a ten years rolling median. (c) scatter-plot of d–θ^{-1} [days] computed on the Euro-Atlantic sector (45°W-45°E) jet positions. Colorscale indicates the percentage of large-scale blocked longitudes. (d) Same as in (c) with waviness (computed as the horizontal jet-position standard deviation) in colors.

Since we can use the latitudinal position of the jet as a relevant index of a blocked situation, we study the behavior of the jet before and after large northward and southward excursions. We focus on the behavior at lon= 0°, but the results are similar when we take another longitude that is often blocked, such as 180°W (not shown). We look at events of northward (southward) excursions of the jet at lon= 0° by imposing that the jet position is above (below) the 85% (15%) quantile of the jet position at lon= 0° for at least 3 consecutive days. These quantiles are chosen to have a sufficient pool of data. The results are not sensitive to a change to the 80% or 90% quantiles (and 20% and 10% quantiles, respectively). We then look at the behavior from 20 days before to 10 days after the northward (southward) excursion.

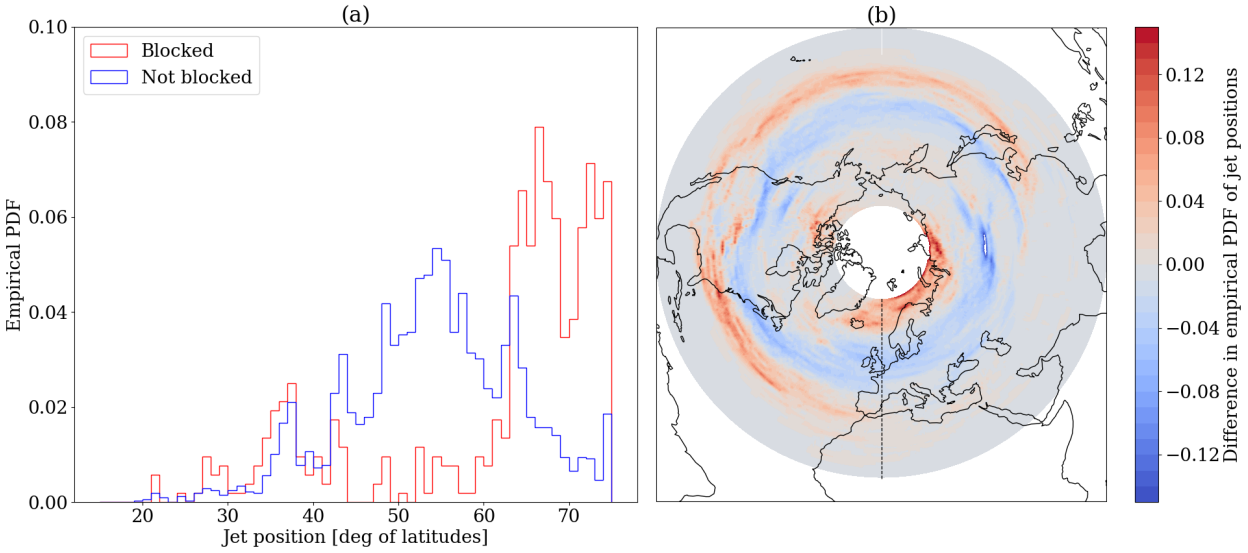

FIG. 6. **Jet position and blocking events.** (a) Empirical probability density of jet positions at lon=0° in the case of blocked and non blocked situations for winter (1979-2019) using Tibaldi and Molteni (1990) large scale blocking index and (b) probability density difference of jet positions in the case of blocked and non blocked situations (red indicates a greater probability of jet position at this latitude in the case of large scale blocking) for all longitudes. The dashed line in panel (b) indicates the cross section at which panel (a) is taken.

Figures 7 and 8 show the composites of northward and southward excursions, containing respectively $n = 73$ and $n = 79$ events. We display the results for four variables: jet latitudinal position, zonal wind speed at 45°N, zonal and meridional wind speed at the jet. All variables are normalized by subtracting their averages and dividing by their standard deviations over all winters longitude by longitude.

Figure 7 panel (a) shows that the northward excursion that we diagnosed has temporal and spatial extensions that are typical of blocking events (respectively 8–9 days and 40° of longitudes, see Lupo (2020)). Panel (d) also shows the positive anomaly east of 0° and negative anomaly west of 0° of meridional wind, so that the structure of the jet looks like so-called omega blocks. We also note on the meridional plot a teleconnection 20 days before the blocking events at 100°W. This longitude corresponds roughly to the location of the Rocky mountains over North America and it is well known that the presence of these mountains intercepting the jet stream can trigger Rossby waves which then travels across the North Atlantic and break near lon= 0° (Kalnay-Rivas

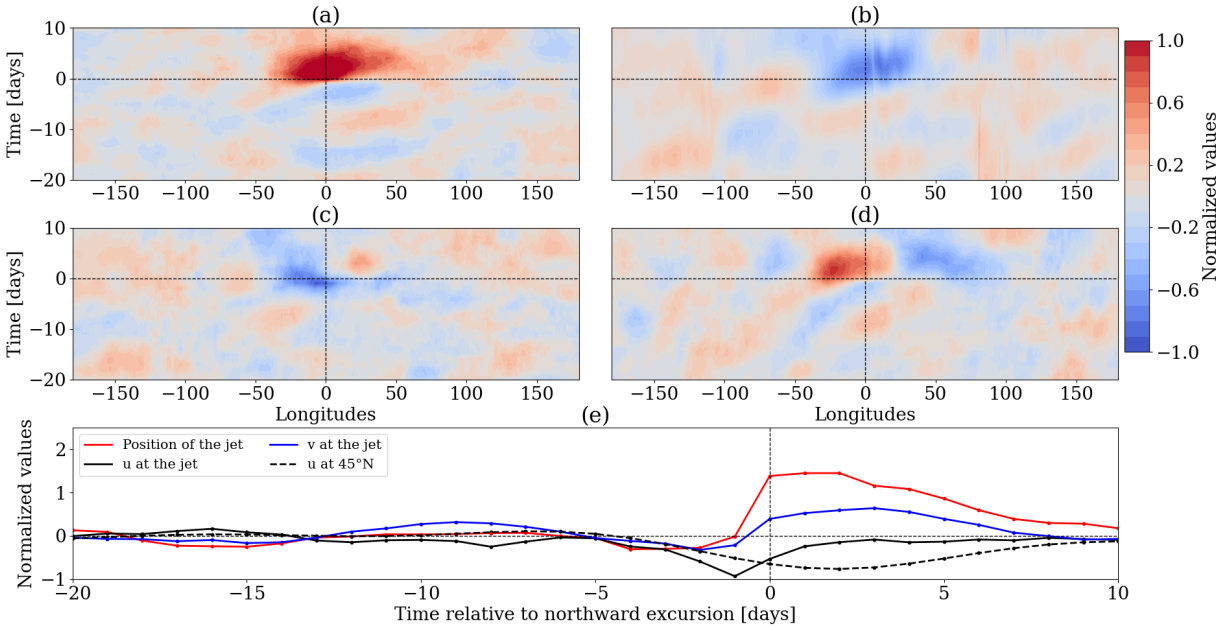

FIG. 7. **Composite behavior during northward excursions of the jet.** Composite mean of n=73 events of northward jet excursions at lon=0° during the winter season: (a) jet position, (b) zonal wind speed at 45°N, (c) zonal wind speed at the jet u_J, (d) meridional wind speed at the jet v_J and (e) cross section of the previous figures at lon=0° (dashed vertical line). All variables are normalized by subtracting their time averages and dividing by their standard deviations. The dashed horizontal lines on panel (a)-(e) show the moment when the northward excursion occurs.

and Merkine 1981). However, the anomaly is weakly positive so that it is not really possible to validate this explanation with our data.

The zonal wind speed at the jet decreases 2–3 days before the northward excursions, whereas the jet position displays no sign of change even the day before its large increase (which means that the "jump" of the jet to a northern position happens at a time scale smaller than a day). The cross section displayed in Figure 7 panel (e) further shows that the zonal wind speed at the jet has a fairly different behavior than the zonal wind speed at 45°N. The former decreases by one standard deviation before the northward jet excursion before reaching the average within 2 days after the jump, whereas the latter decreases when the jet jumps and remains negative 5–10 days after that, which is coherent with a northern position of the strong zonal winds of the jet.

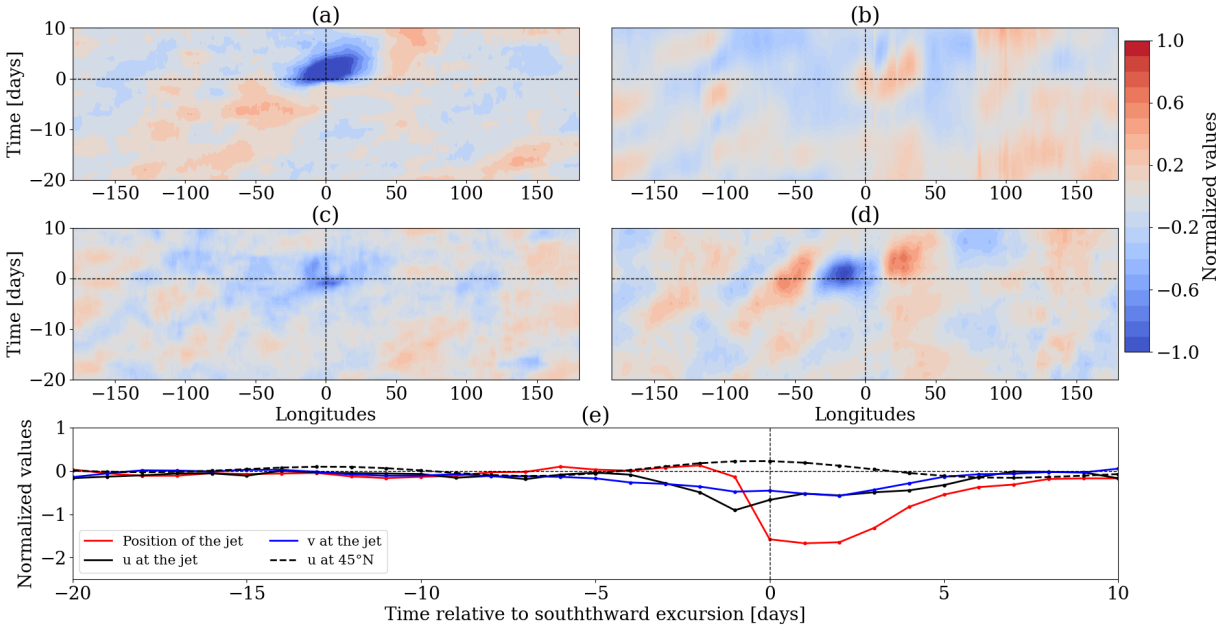

FIG. 8. **Composite behavior during southward excursions of the jet.** Composite mean of $n = 79$ events of southward jet excursions at lon=0° during the winter season: (a) jet position, (b) zonal wind speed at 45°N, (c) zonal wind speed at the jet u_J, (d) meridional wind speed at the jet v_J and (e) cross section of the previous figures at lon=0° (dashed vertical line). All variables are normalized by subtracting their time averages and dividing by their standard deviations. The dashed horizontal lines on panel (a)-(e) show the moment when the southward excursion occurs.

To ensure that this excursion corresponds to a blocking event, we display in Figure 9 the composite anomaly of zonal wind, jet position and geopotential height at 500 hPa (Z500) from 4 days before to 4 days after the northward excursion of the jet over the entire northern hemisphere. The strong negative anomaly of zonal wind over Europe, the positive anomaly of zonal wind between Iceland and Norway and the characteristic wave breaking footprint of Z500 isolines are all elements that show a switch from a mostly zonal to a mostly meridional jet, therefore a blocked state. This mostly meridional state of the jet is confirmed by Figure 10 which is similar to Figure 9 with the meridional wind speed in colors.

Figure 8 displays different results from Figure 7 for southward excursions of the jet at 0°. First, the spatial and temporal extensions of the southward excursions are a bit smaller than for the northward excursions. Secondly, the structure of the meridional wind after the excursion is

not dipolar (negative anomaly – positive anomaly) but tripolar: with a positive meridional wind anomaly approximately 70° of longitudes west of 0°, then a negative anomaly west of the excursion and finally a positive anomaly east of the excursion. Finally, zonal wind speed at 45°N does not decreases but rather increases during the excursion, and the amplitude of the anomaly is not as big. The common point is that there is also a weakening of the zonal wind speed at the jet 2–3 days before the excursion. Figures 11 and 12 confirm this analysis for the behavior of the jet over all the northern hemisphere during large southward excursions of the jet. The structures displayed in these figures are rather different from the traditional omega blocking shape, as if the blocking event was occurring 15°west of the central longitude 0° and the southward excursion of the jet at 0° was a consequence of this more western blocking. The structure seems to be more similar with the so-called Atlantic blocking pattern (Vautard 1990).

To check that the observed slowdown in the zonal wind speed before large northward and southward excursions of the jet is statistically significant, we compute the 95% confidence interval using 1000-iterations bootstrap on the sample of events. The results are displayed in Figure 13 and show the significance of this precursory slowdown.

c. Point stochastic model

We have shown that strong excursions of the jet, either in the northward or southward direction, can be characterized as blocking events. Moreover, we have shown that large "jumps" of the jet from a central position to either the north or south, leading to blocking events, are closely linked to a decrease in the zonal wind speed measured at the jet position 2 to 3 days before the jump, as is found by the literature: Woollings et al. (2018b) showed that a decrease in the zonal wind is associated with a higher variability of the jet, and Nakamura and Huang (2018) showed that blocking events are characterized by high values of local wave activity (Huang and Nakamura 2016) which is itself negatively correlated with zonal wind speed. As we want to derive a 1D model for the onset and decay of blocking events on the jet, we focus on the behavior of the zonal wind speed at the jet u_J. In the following, apart when specified so, all analyses are made with winter data.

To do so, we plot in Figure 14 panel (a) the phase portrait of the zonal wind speed u_J at the jet. The temporal derivative $\frac{du_J}{dt}$ is computed as $\frac{du_J}{dt} = u_J(t+1) - u_J(t)$, as dt is set to be equal

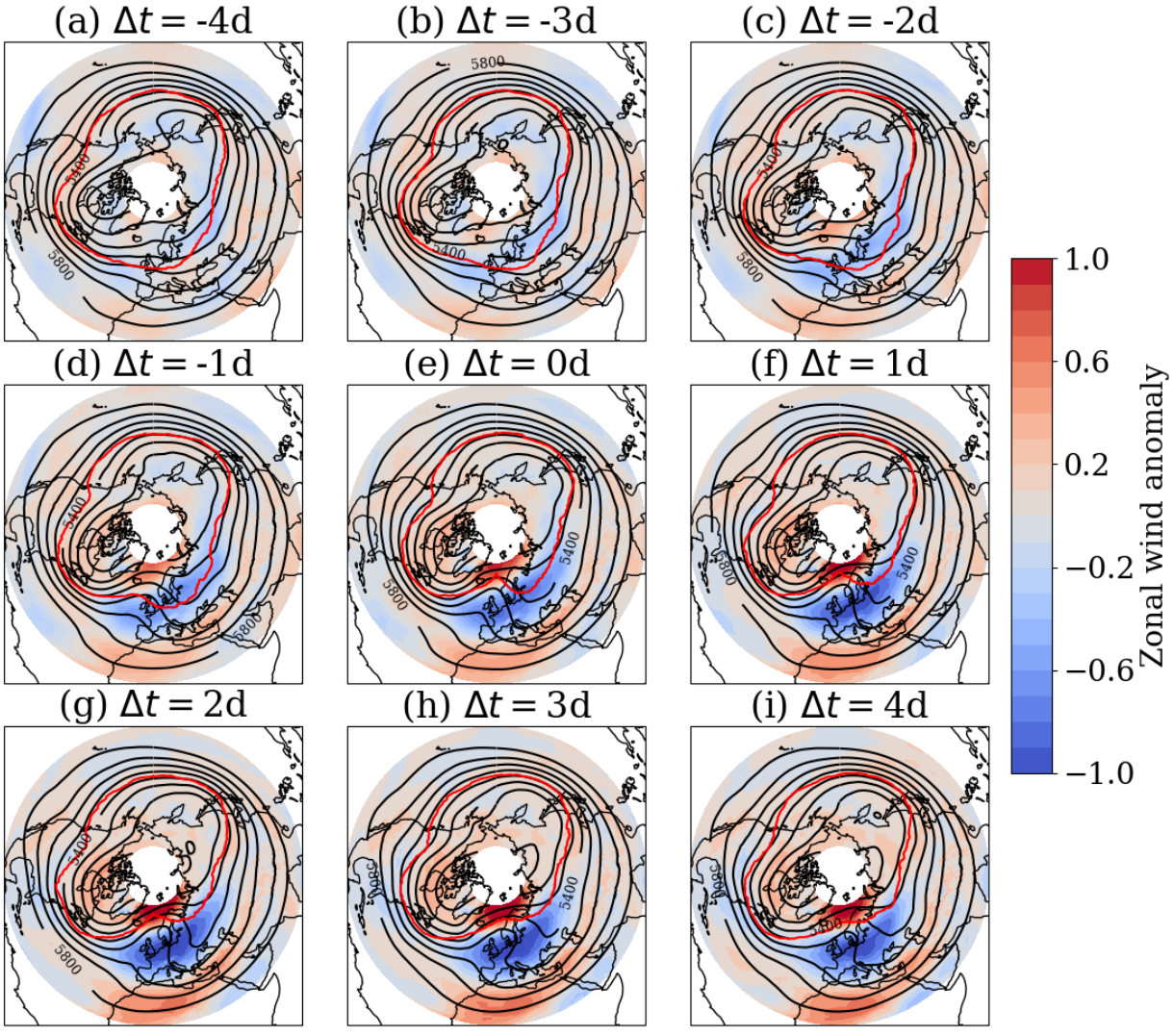

FIG. 9. **Composite behavior of zonal wind (normalized) and geopotential height (m) during northward excursions over the Northern Hemisphere.** Composite anomaly of zonal wind (colors), jet position (red line) and Z500 (black lines) from 4 days before to 4 days after the northward excursion of the jet (n=73 events). Z500 lines are traced every 100m from 5000 m to 6000 m.

to 1 day. Apart from outliers, the bulk of points is located within the interval $[-2, 2]$ and has an elliptic shape, so that u_J seems to display an oscillator-like structure. Figure 14 panel (b) shows the relation between $\frac{d^2u_J}{dt^2}$ and u_J. For an oscillator, either linear or non-linear, we would have $\frac{d^2u_J}{dt^2} = F(u_J)$ with $xF(x) < 0$. In this analysis the double temporal derivative is computed as:

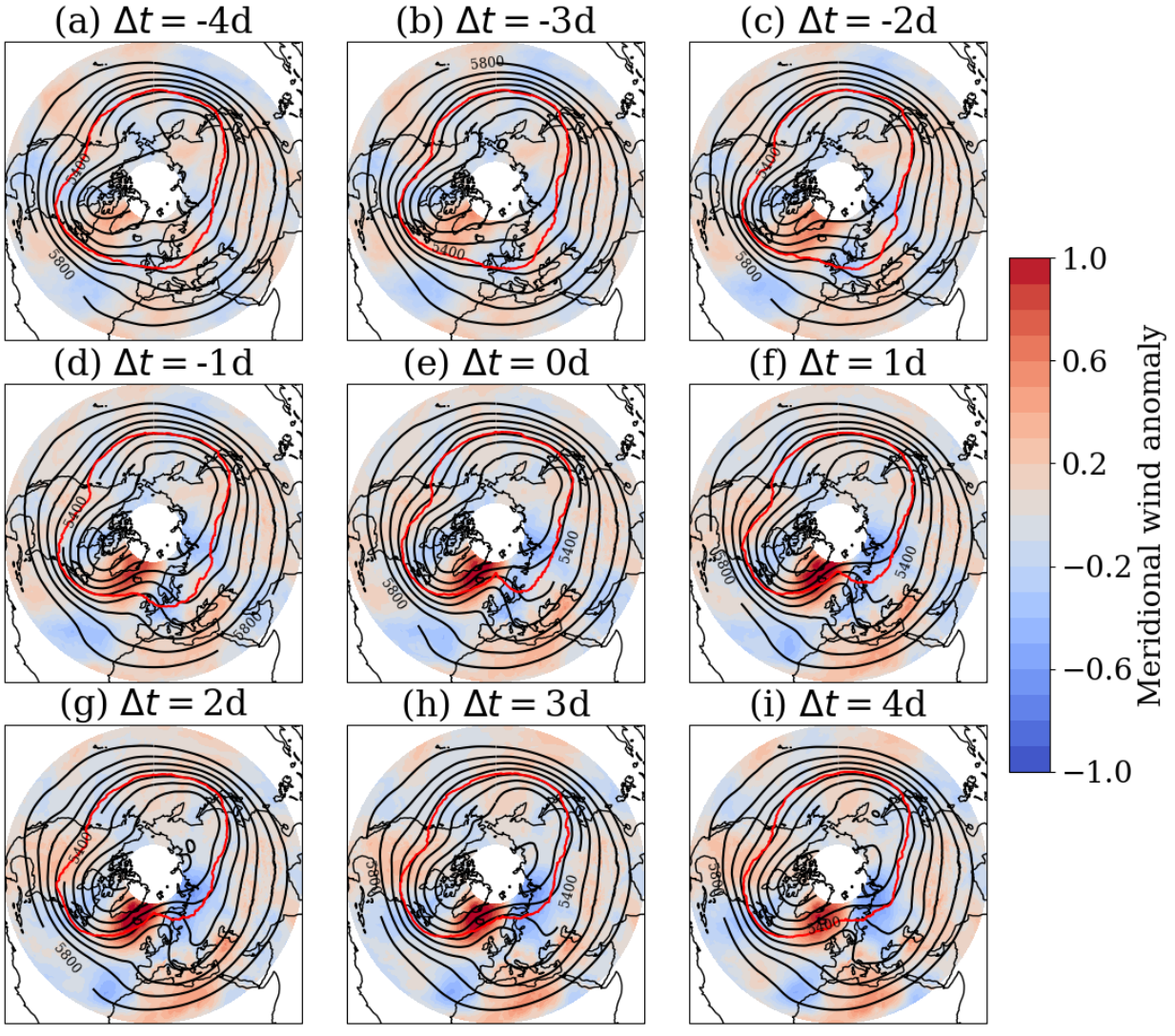

FIG. 10. **Composite behavior of meridional wind (normalized) and geopotential height (m) during northward excursions over the Northern Hemisphere.** Composite anomaly of meridional wind (colors), jet position (red line) and Z500 (black lines) from 4 days before to 4 days after the northward excursion of the jet ($n = 73$ events). Z500 lines are traced every 100m from 5km to 6km.

$$\frac{d^2 u_J}{dt^2} = u_J(t+1) - 2u_J(t) + u_J(t-1).$$

Again, there are several outliers in the data points, but we recall that approximately 3500 points are drawn in this figure, so that the vast majority of them is located within the interval $[-2, 2]$. It

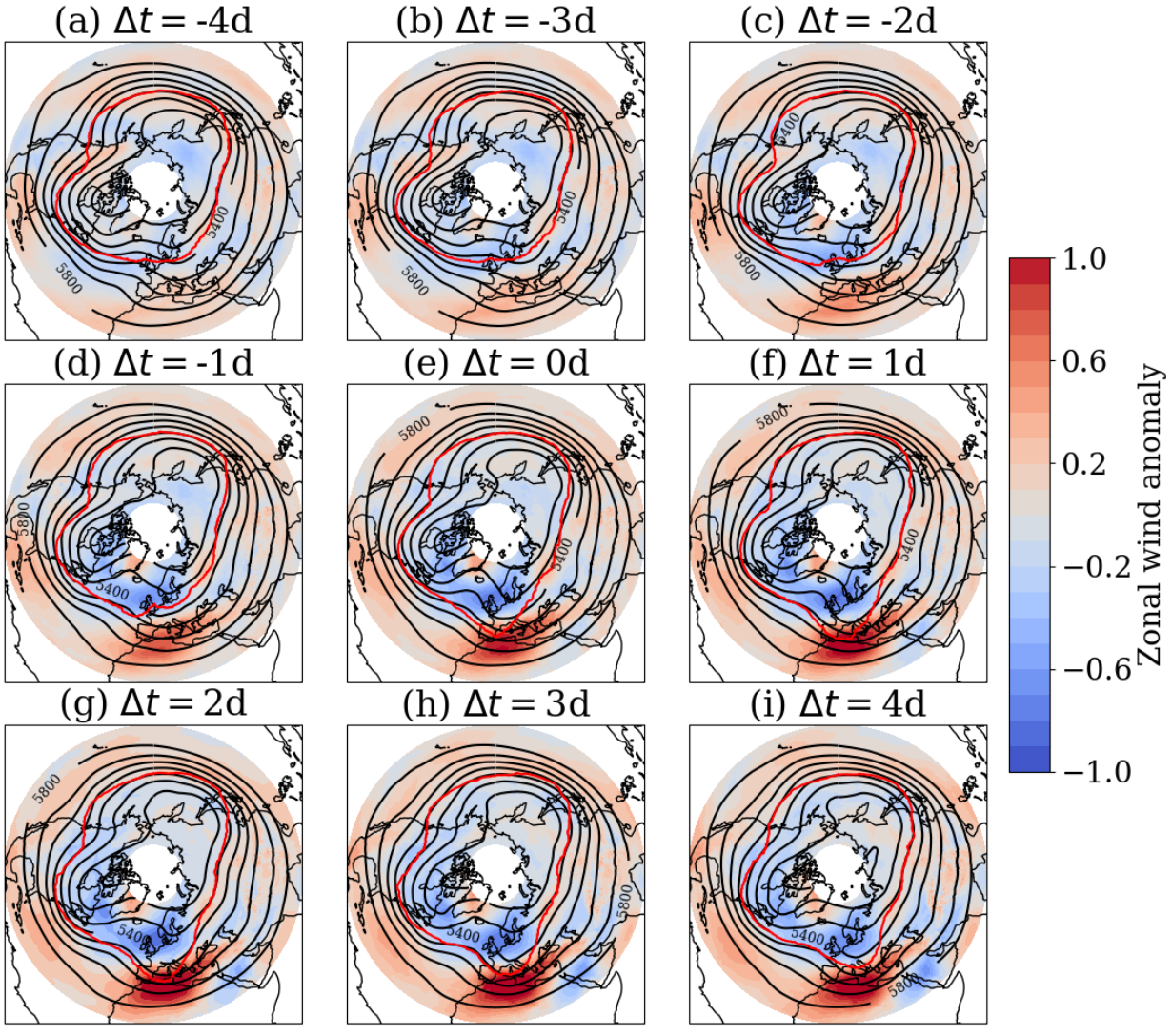

355 FIG. 11. **Composite behavior of zonal wind (normalized) and geopotential height (m) during southward**
356 **excursions over the Northern Hemisphere.** Composite anomaly of zonal wind (colors), jet position (red line)
357 and Z500 (black lines) from 4 days before to 4 days after the southward excursion of the jet ($n = 79$ events). Z500
358 lines are traced every 100m from 5000 m to 6000 m.

394 is also clear that there is a strong asymmetry relative to the y-axis. While many functions would
395 fit those data, we choose an exponential-like model

$$F_{a,b}(x) = a(e^{-bx} - 1).$$

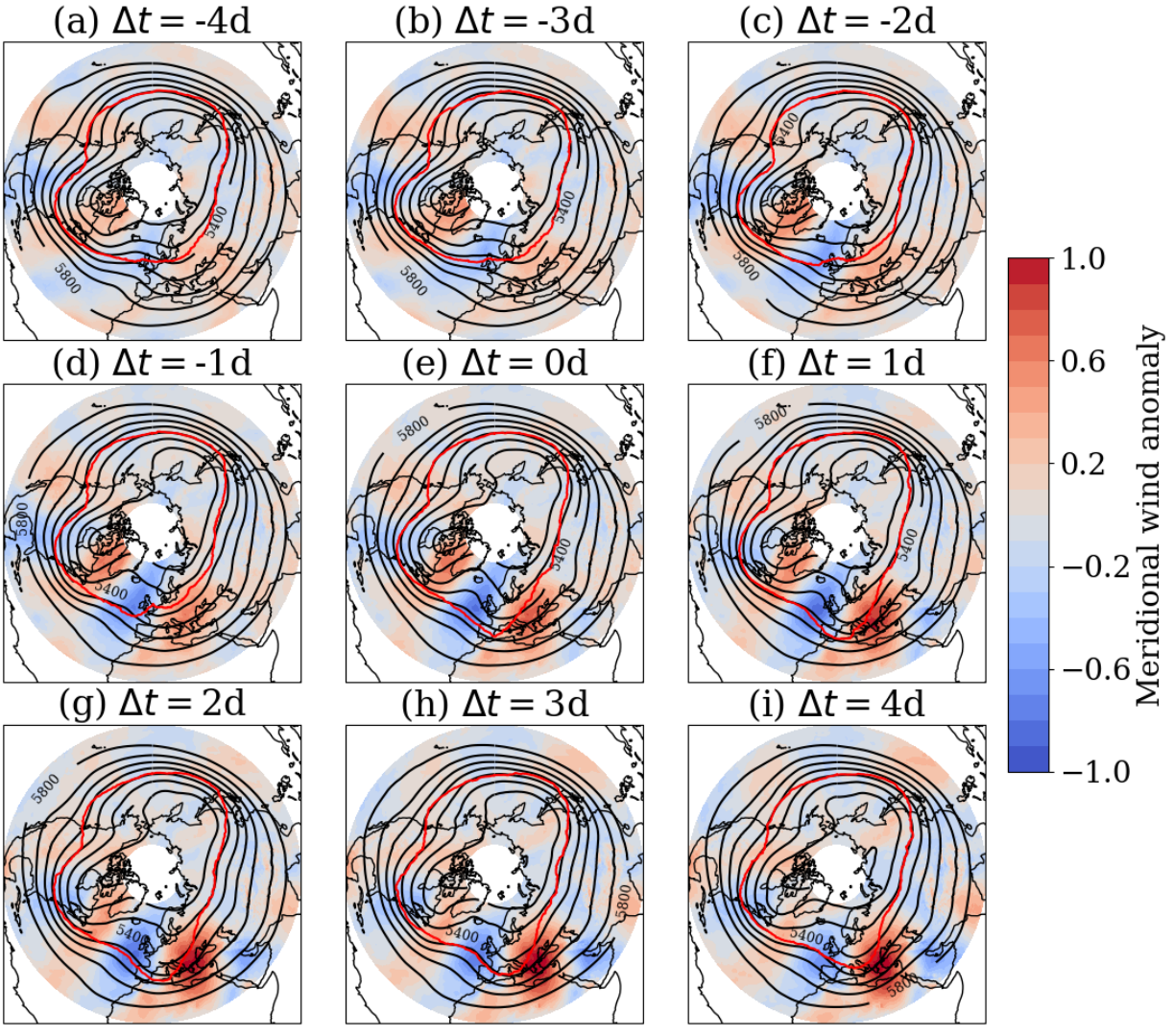

359 FIG. 12. **Composite behavior of meridional wind (normalized) and geopotential height (m) during**
360 **southward excursions over the Northern Hemisphere.** Composite anomaly of meridional wind (colors), jet
361 position (red line) and Z500 (black lines) from 4 days before to 4 days after the southward excursion of the jet
362 ($n = 79$ events). Z500 lines are traced every 100m from 5000 m to 6000 m.

396 We fit the parameters by minimizing the Euclidean distance between the model and the data. We
397 find parameter value $a = 0.27$ and $b = 0.77$. To alleviate notations, we will write simply u (rather
398 than u_J) the zonal wind speed at the jet in the remainder of the article.

399 The proposed model corresponds to a non-linear oscillator evolving in a potential well $V_{a,b}(x) =$
400 $a\left(\frac{1}{b}e^{-bx} - x\right)$, so that its total energy $E = \frac{1}{2}\left(\frac{du}{dt}\right)^2 + V(u)$ is preserved. However, a standard

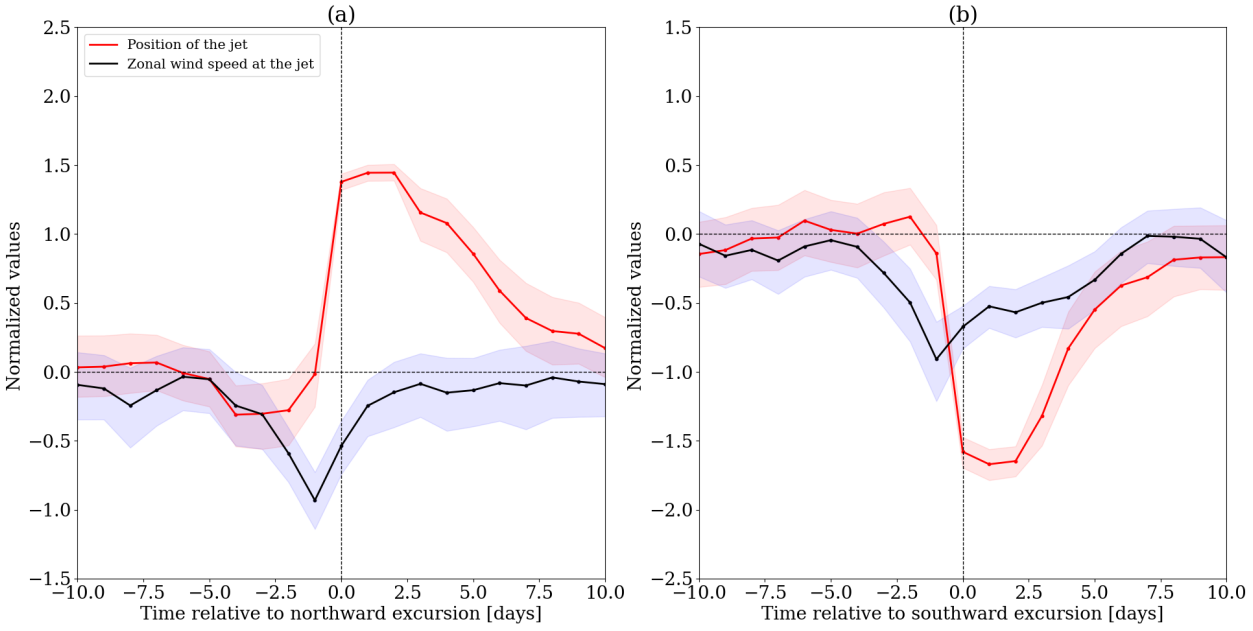

FIG. 13. **Composite of jet position (red) and zonal wind speed at the jet (blue) for large (a) northward and (b) southward jet excursions (respectively $n = 73$ and $n = 79$).** The shaded areas represent the 95% confidence interval computed using 1000-iterations bootstrap on the sample of events.

oscillator should display regular oscillations, which is not the case in Figure 14. Therefore, we add a stochastic term to represent perturbations. In the end, we propose the following model for the behavior of jet zonal wind speed u at the jet at lon= 0°:

$$\frac{d^2u}{dt^2} = F_{a,b}(u) + \eta(t) - \alpha\frac{du}{dt}, \tag{2}$$

where $F_{a,b}$ is the function defined above, η is a white noise with standard deviation σ and $-\alpha\frac{du}{dt}$ is a damping term added to avoid instability (η brings too much energy in the system). Figure 15 panel (a) displays 3 winters example (2000-2003), comparing the normalized zonal wind speed (black) and the proposed stochastic model (red). The model is integrated using a fourth-order Runge-Kutta scheme with a time step of 0.1 day and the forcing is applied at every time step. We found $\sigma = 0.35$ and $\alpha = 0.1$ to fit reasonably well the data by a semi-objective inspection of the results without performing an objective parameter optimisation, that would be left for a future study. Figure 15 panel (c) displays the comparison between the two histograms. The model is very close to the data in the range $[-2, 2]$, but overestimates the proportion of high winds ($u > 2$)

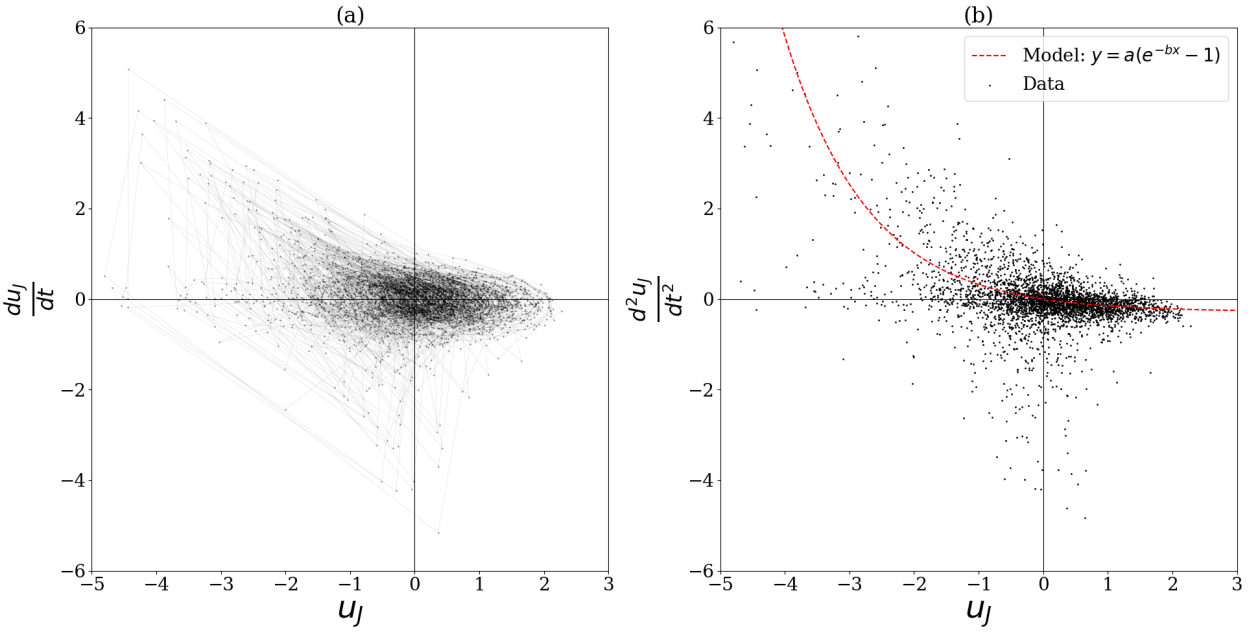

FIG. 14. **Dynamical behavior of zonal wind speed at the jet.** (a) Phase portrait of zonal wind speed at the jet u_J at lon=0° and (b) relation between $\frac{d^2u_J}{dt^2}$ and u_J at lon=0° (points) and proposed model (red). The red model is fitted using points such that $|u_J| < 2.5$ and $\frac{d^2u_J}{dt^2} > -0.8$ to remove outliers. By minimizing the euclidean distance between the model and the data we find $a = 0.278$ and $b = 0.771$.

and underestimates the proportion of low winds ($u < -2$). This is not an issue because (i) for low winds, as we have seen above, a slight slowdown of zonal wind is enough to trigger transition to a blocked state, so that there is no need to go below $u = -2$ — moreover one has to take into account that those values may be outliers and not a physical feature as we don't look at temporal and spatial means — and (ii) for high winds, $u > 1$ is already associated with a zonal jet so that when u takes bigger values there is no further influence on the position of the jet.

Since our main purpose is to build a model for blocked states, we propose the following forced Langevin equation for the jet position X at lon=0°:

$$\frac{dX}{dt} = -\beta X + F(X,u) + \eta'(t), \tag{3}$$

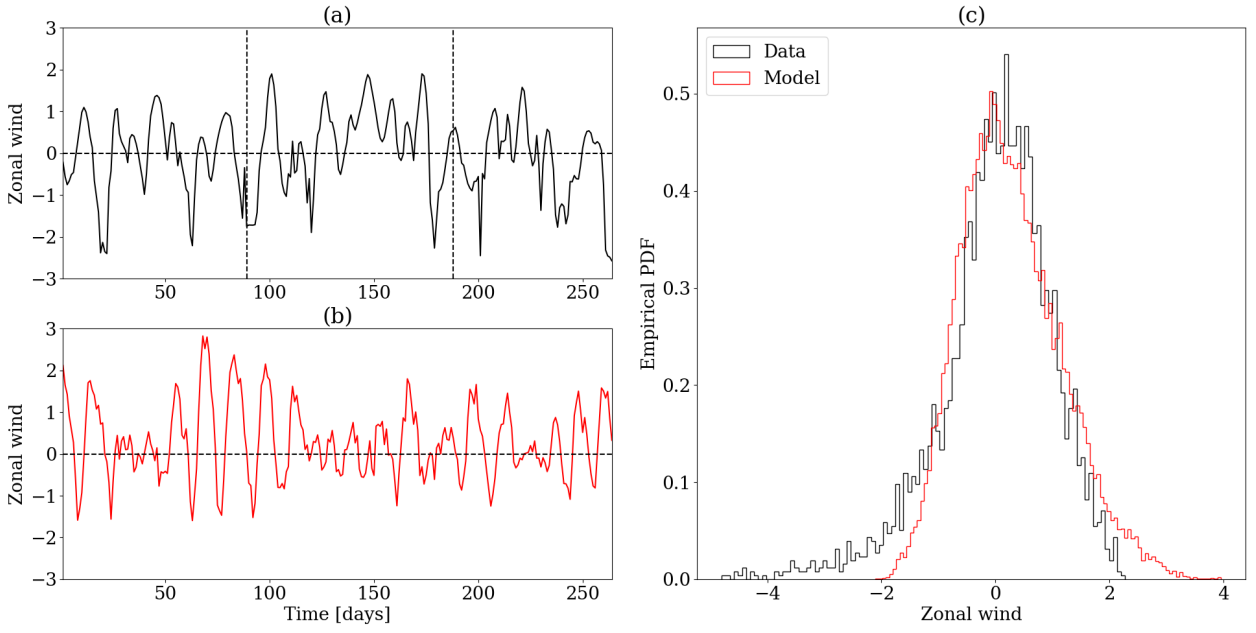

FIG. 15. **Point model for the zonal wind speed at the jet.** (a) Normalized zonal wind speed at lon=0° over three winters (2000-2003) (black) and proposed stochastic model (red) and (b) comparison of the histograms for the data (black) and the model (red). Vertical black dashed lines in panel (a) represent the limits between the three winters for the data, so that there is no continuity in the black lines at those times. The model is computed at a 0.1 day time step over 10 years but is plotted every 10 time steps (one day) to be comparable to the data.

where β is fitted to Figure 13 so that we find $\beta^{-1} = 10$ days, $F(X,u)$ is a forcing term defined as follows:

$$F(X,u) = \begin{cases} C(|u| - |X|)sign(X) & \text{if } u < 0 \text{ and } |X| < |u|, \\ 0 & \text{otherwise ,} \end{cases} \tag{4}$$

so that the forcing is null when the jet zonal wind speed is strong ($u > 0$) and is linearly forced when the jet zonal wind speed is weak ($u < 0$), which is consistent with the negative correlation between the jet zonal wind speed and the jet position variability investigated by Woollings et al. (2018b) (see in particular their Figure 1). Multiplying by the sign of X, combined with the random perturbation, allows the model to display northward and southward excursions of the jet. The rationale of this operation is that if the jet is already anomalously high/low, it tends to stay there. The condition $|X| < |u|$ allows to take into account the fact that the forcing is asymmetric, as can

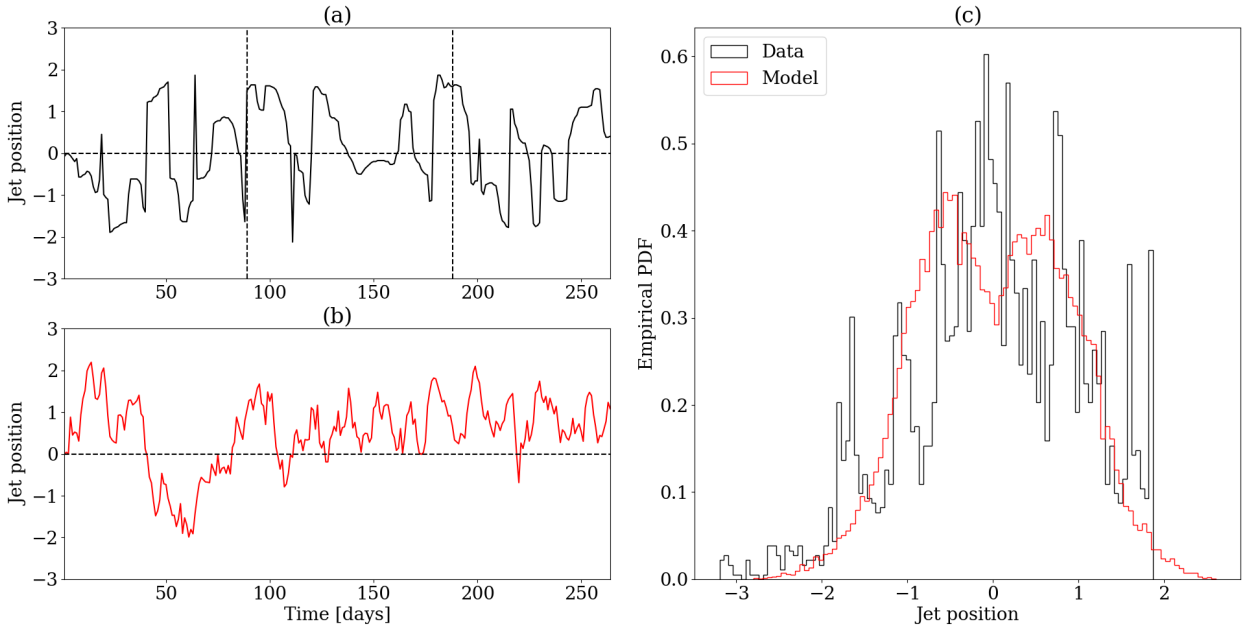

FIG. 16. **Point model for the jet position.** (a) Normalized jet position at lon=0° over three winters (2000-2003) (black) and proposed stochastic model (red) and (b) comparison of the histograms for the data (black) and the model (red). Vertical black dashed lines in panel (a) represent the limits between the three winters for the data, so that there is no continuity in the black lines at those times. The model is computed at a 0.1 day time step over 10 years but is plotted every 10 time steps (one day) to be comparable to the data.

be seen in Figure 13: when u is decreasing the jet latitude drifts away from the central position, but the relaxation period when u increases again does not see immediately a come back of the jet to its central position. We choose $C^{-1} = 1$ day to be the time scale of increase for the forcing, as in figure 13. Finally η' is a white noise with standard deviation $\sigma' = 0.35$ as for u. The proposed model is close to a modified red noise model: $X_{t+1} = \mu_t + \phi X_t + \epsilon_t$, where μ_t is the moving average, the equivalent of our forcing. In our case, with a constant forcing $u < 0$, we would have two equilibrium positions: $X^1_{eq} = \frac{C}{\beta+C}|u| \simeq |u|$ and $X^2_{eq} = -\frac{C}{\beta+C}|u| \simeq -|u|$.

The results for the stochastic model are displayed in Figure 16. Even though the jet has a tendency not to stay at anomalously high or low positions as in the data, the model is able to reproduce the large and sudden shifts of the jet.

To conclude this section, we note that the analysis provided here using the zonal wind "sitting" on the jet is different from that one obtained at a fixed latitude, for example at 45°N as illustrated in

Figure 17. Panel (a) shows the relation between $\frac{d^2u_{45N}}{dt^2}$ and u_{45N} and Figure 17 panel (b) displays the wavelet spectrum of the zonal wind at the jet u, at 45°N u_{45N}, for the model and for a red noise computed using parameters that best fit the data for each winter. For the wavelet spectrum of the data, either at the jet or at 45°N, we used the full data set over the 40 years and then we aggregated the amplitudes for winter times. We show the spectrum only up to a period of 100 days but the main peak of the spectrum is of course located at 365 days. A red noise is fitted for each of the 40 winters and the spectrum is computed as the aggregation of the 40 spectra. One striking feature of this spectrum is that, contrary to the zonal wind speed at 45°N which displays two local maxima (at 27 and 49 days), zonal wind speed at the jet displays four local maxima (at 17, 22.5, 38 and 74.5 days), which correspond to temporal properties of the series as is shown with the difference with a corresponding red noise spectrum. Those maxima are typical of the time scales associated with the Rossby waves propagating in the atmosphere at these latitudes (Hoskins and James 2014). The spectrum associated with the model does not fit with the one of the data. The main reason for that is that the model is a simple 0D model without spatial interactions. The goal of the next section is therefore to propose a model with spatial interactions that could explain those features.

4. Spatially extended model: coupled non-linear oscillators and Toda lattice

In the previous section we proposed a 0D model for the zonal wind speed at the jet u and for the jet latitudinal position X at lon=0°. In this section, we extend this model along all longitudes i. The basic idea is to assume that the jet zonal wind speed at each longitude can be represented as a material point in the potential well $V_{a,b}(x) = a(\frac{1}{b}e^{-bx} - x)$ defined above. Our idea is then to introduce a coupling between those oscillators (see Figure 18). For any oscillator, the force applied by the oscillator on its right is: $-F_{a,b}(u^{i+1} - u^i)$, whereas the force applied on its left is: $F_{a,b}(u^i - u^{i-1})$. So that the dynamics of the oscillator is:

$$\frac{d^2u^i}{dt^2} = F_{a,b}(u^i - u^{i-1}) - F_{a,b}(u^{i+1} - u^i) = a\left(e^{-b(u^i - u^{i-1})} - e^{-b(u^{i+1} - u^i)}\right) \tag{5}$$

and we have a periodic string of oscillators so that: $u^{i+N} = u^i$. This coupled dynamics is known as the Toda lattice and has been used to model interaction between electrons in a solid (Toda 1967). The advantage of using a function which gives the Toda lattice is that this system can be

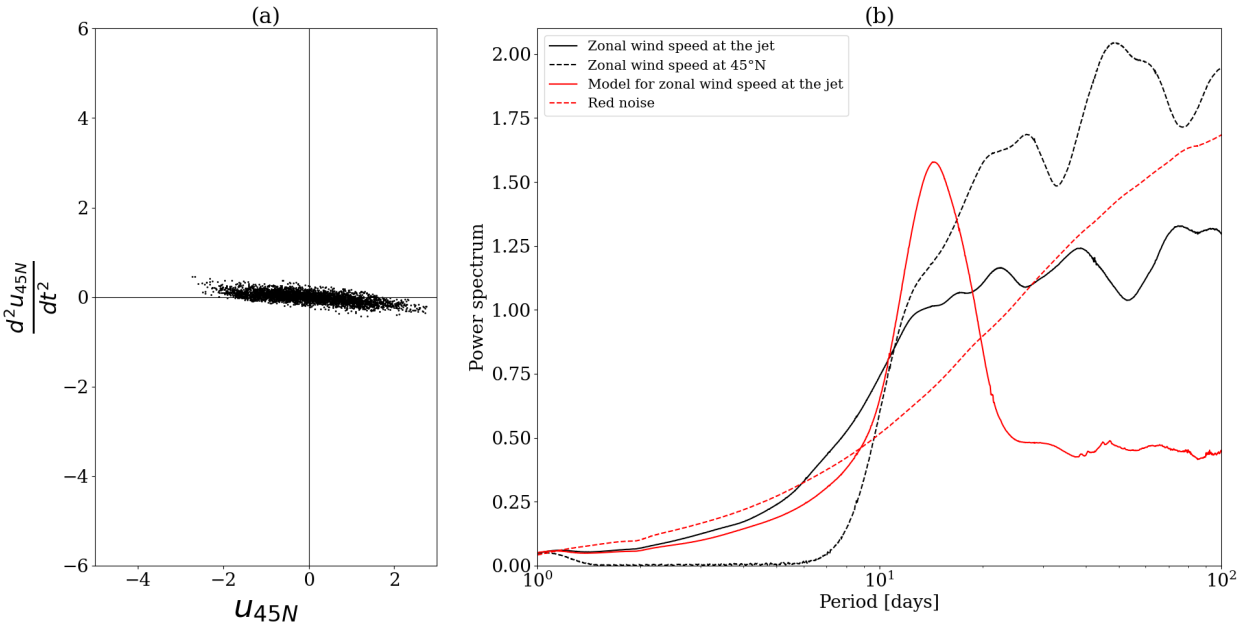

FIG. 17. **Comparison of the analysis at the jet and at a fixed latitude.** (a) Relation between $\frac{d^2u_{45N}}{dt^2}$ and u_{45N} at lon=0° and (b) wavelet power spectrum of zonal wind speed at the jet (black plain line), zonal wind speed at 45°N (black dashed line), model for the zonal wind speed at the jet (red plain line) and a red noise whose parameters are fitted to the series of zonal wind speed at the jet data (red dashed line).

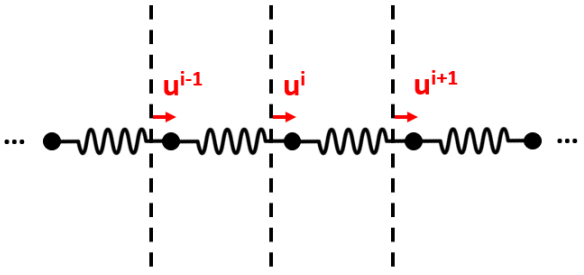

FIG. 18. **Schematic of the spatial model as coupled oscillators.** u^i represents the position of the oscillator i with respect to its equilibrium position.

derived from a Hamiltonian and therefore its total energy is conserved, which makes it very stable, especially for numerical simulations (Toda 1975).

Figure 19 presents the result of this model with 1440 oscillators (the number of longitude grid points in the data) for $a = 200$ and $b = 2$, initiated with random values taken from a uniform distribution over $[-c, c]$ with $c = 0.4$ and integrated using a fourth-order Runge-Kutta scheme with

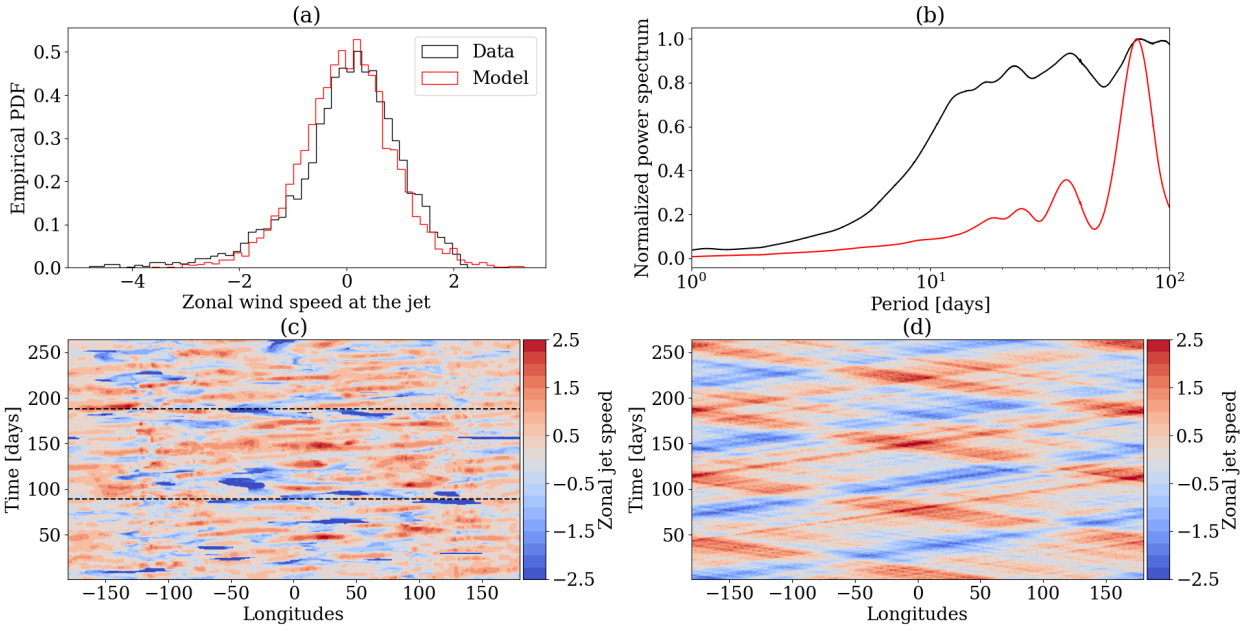

FIG. 19. **Unperturbed spatial model for zonal wind speed at the jet.** (a) Histograms at lon=0° of zonal wind speed at the jet for the data (black) and the model (red). (b) Normalized wavelet power spectrum for the data (black) and the model (red). The power spectrum is normalized by dividing by the greatest value of the spectrum over the range of periods 1-100 days. (c) Hovmöller diagram of zonal wind speed at the jet for the data over three winters (2000–2003). Horizontal dashed lines represent the limits between the three winters for the data, so that there is no continuity at those times. (d) Hovmöller diagram of zonal wind speed at the jet for the model over three winters. The model is computed at a 0.01 day time step over 10 years but is plotted every 100 time steps (one day) to be comparable to the data.

a time step of 0.01 day over 10 years (3.65×10^5 time steps). The values of a, b and c were found using a trial-and-error procedure to fit the data on the histogram, the wavelet spectrum and the horizontal wavelength on the Hovmöller diagram. We find that the model succeeds in fitting those diagrams, especially for the wavelet spectrum, which shows a series of peaks similar to the one observed in the data (even though the periods corresponding to the peak are not perfectly identical). Similarly, the model is able to represent propagating waves seen in the data, albeit with too much emphasis on eastward propagating waves. The values for a and b are different from the ones proposed in the point model (respectively $a = 0.278$ and $b = 0.771$). This is justified by the fact that they are used here in a very different settings due to the coupling between the oscillators.

As in the model proposed by Faranda et al. (2019), we need to take into account the stochastic disturbances applied by baroclinic and barotropic motions, wave breaking events, convective processes and other sub-grid processes on the jet. As proposed by Barnes and Hartmann (2011) and supported by Woollings et al. (2018b), a purely barotropic model of the atmosphere can represent such a variability of the jet due to barotropic Rossby wave breaking on each of its sides. Therefore the proposed stochastic disturbances could be considered to represent only this mechanism on the jet zonal wind speed variability. For that, similar to Vallis et al. (2004) (see also Paradise et al. (2019) who took a similar approach with the 1D model proposed by Nakamura and Huang (2018)), we apply the following stochastic noise:

$$S^i(t) = \frac{\gamma}{N} \sum_{n=1}^{N} w_n(t) \cos\left(\frac{2\pi k_n}{L} i + \phi_n(t)\right), \tag{6}$$

where γ controls the intensity of the noise, N is the number of horizontal wave numbers on which the system is perturbed, $L = 1440$ is the number of oscillators, k_n are the horizontal wave numbers on which the system is forced and we take $k_n = 20$ to 30 to stick with the typical horizontal scale of weather disturbances (as in Faranda et al. (2019)). Finally, to ensure time consistency, amplitudes $w_n(t)$ and phases $\phi_n(t)$ follow an Ornstein-Uhlenbeck stochastic process that we approximate in discrete time by:

$$\begin{cases} w_n(t+dt) = (1 - e^{-2dt/\tau})^{\frac{1}{2}} Q_n + e^{-dt/\tau} w_n(t), \\ \phi_n(t+dt) = (1 - e^{-2dt/\tau})^{\frac{1}{2}} Q'_n + e^{-dt/\tau} \phi_n(t), \end{cases} \tag{7}$$

where τ is the decorrelation time that we choose to be equal to 2 days, $dt = 0.01$ the time step of integration of the model and Q_n and Q'_n random numbers chosen at each time step from a uniform distribution over respectively $[-\delta, \delta]$ with $\delta = 0.1$ and $[-\pi, \pi]$. $w_n(0)$ and $\phi_n(0)$ are taken randomly from a uniform distribution over respectively $[-\delta, \delta]$ with $\delta = 0.1$ and $[-\pi, \pi]$.

To ensure that the model is numerically stable, we also add a damping term $-\alpha \frac{du^i}{dt}$, so that in the end, we have:

$$\frac{d^2u^i}{dt^2} = a(e^{-b(u^i - u^{i-1})} - e^{-b(u^{i+1} - u^i)}) + S^i - \alpha \frac{du^i}{dt}. \tag{8}$$

Figure 20 presents the results for the perturbed model with $\gamma = 0.3$ and $\alpha = 0.05$, which we found to be a good compromise to fit the data by a trial-and-error procedure. The model is integrated using a fourth-order Runge-Kutta scheme with a time step $dt = 0.01$ day and the forcing is applied at each time step over a period of 10 years. Apart from the local maximum for periods below 10 days in the wavelet spectrum in panel (b), the model reproduces the spectrum observed in the data at lon=0°, especially the shape and the position of the three local maxima for periods greater than 10 days. The temporal spectrum for longitudes close to 0° (20°W-20°E) is similar to the displayed spectrum — with peaks at 23 and 40 days and a trough around 52 days — so that this result is not sensitive to the particular choice of longitudes. Therefore, the temporal waves present in the model are closed to the ones of the data as is also confirmed when comparing panel (c) and panel (d). There are two main differences in those plots: (i) the propagating speed either in the westward or eastward direction is larger in the model than in the data and (ii) the temporal spectrum displays local maxima for periods below 10 days, which correspond to the added perturbation S^i.

Finally, we propose to adapt the 0D forced Langevin equation of the previous section to model the latitudinal position of the jet:

$$\frac{dX^i}{dt} = -\beta X^i + F(X^i, u^i) + \hat{S}^i + D(X^{i+1} - 2X^i + X^{i-1}), \tag{9}$$

where $\beta^{-1} = 10$ days, $F(X^i, u^i)$ is the same forcing as previously:

$$F(X^i, u^i) = \begin{cases} C(|u^i| - |X^i|)sign(X^i) & \text{if } u^i < 0 \text{ and } |X^i| < |u^i|, \\ 0 & \text{otherwise,} \end{cases} \tag{10}$$

where $C = 1$, $\hat{S}^i$ is a source term defined the same way as S^i above but we take $\gamma = 0.6$ and $k_n = 2$ to 8 to take into account the greater spatial coherence of the jet position than the zonal wind speed and the last term on the right hand side is a diffusion term, to smooth the position of the jet, with $D = 20$. Again, the model is integrated using a fourth-order Runge-Kutta scheme with a time step $dt = 0.01$ day and the forcing is applied at each time step over a period of 10 years.

Figure 21 presents the results for the spatial model of the jet position. On Figure 21 panel (a) we present the comparison between the histograms of the model and the data at lon=0°, whereas panels (b), (c) and (d) present Hovmöller diagrams of jet position for the data, for jet zonal wind speed

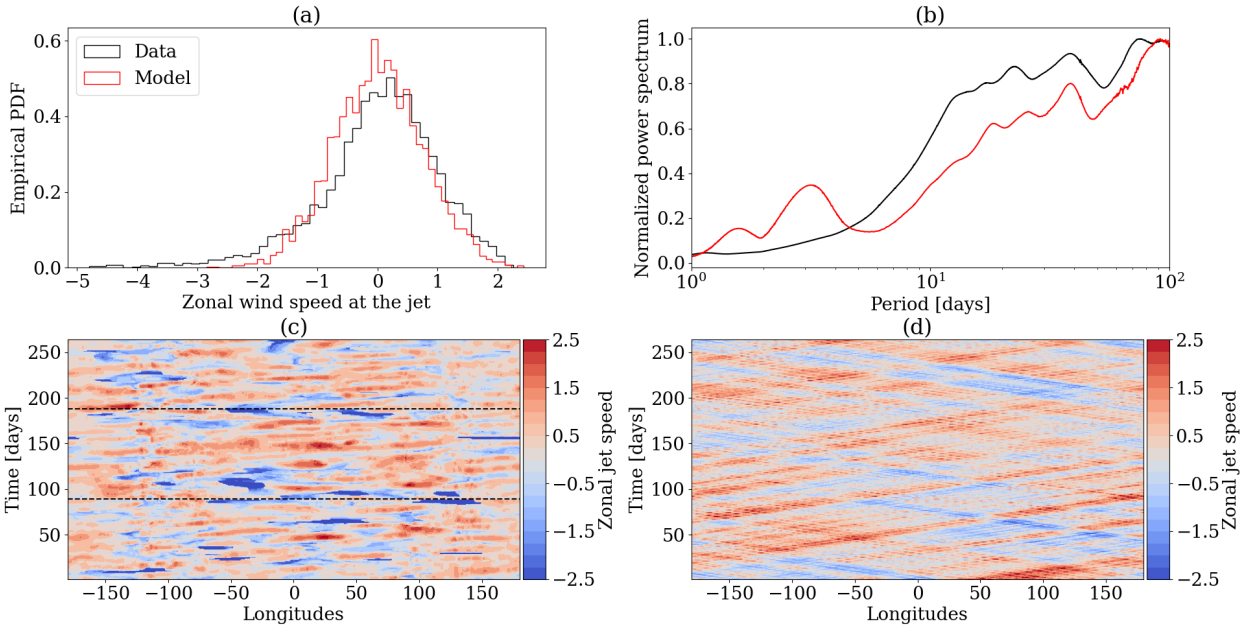

FIG. 20. **Perturbed spatial model for zonal wind speed at the jet.** (a) Histograms at lon=0° of zonal wind speed at the jet for the data (black) and the model (red). (b) Normalized wavelet power spectrum for the data (black) and the model (red). The power spectrum is normalized by dividing by the greatest value of the spectrum over the range of periods 1-100 days. (c) Hovmöller diagram of zonal wind speed at the jet for the data over three winters (2000-2003). Horizontal dashed lines represent the limits between the three winters for the data, so that there is no continuity at those times. (d) Hovmöller diagram of zonal wind speed at the jet for the model over three winters. The model is computed at a 0.01 day time step over 10 years but is plotted every 100 time steps (one day) to be comparable to the data.

of the model and corresponding jet latitudinal position in the model. The model for the latitudinal jet position reproduces the large northward and southward excursions corresponding to low values of the jet zonal wind speed as can be seen comparing panels (c) and (d). Even though the jet latitudinal position in the model displays spatial extensions coherent with the data, the temporal coherence of the model seems too large compared to ERA5 data, where there is more sudden shifts in the jet position that we were not able to obtain. Given that the variability of our model is assured by the combination of the random noise and the sign of X in front of the forcing term in equation 9, the reason could be that the value of γ taken to model the strength of disturbances is not large enough.

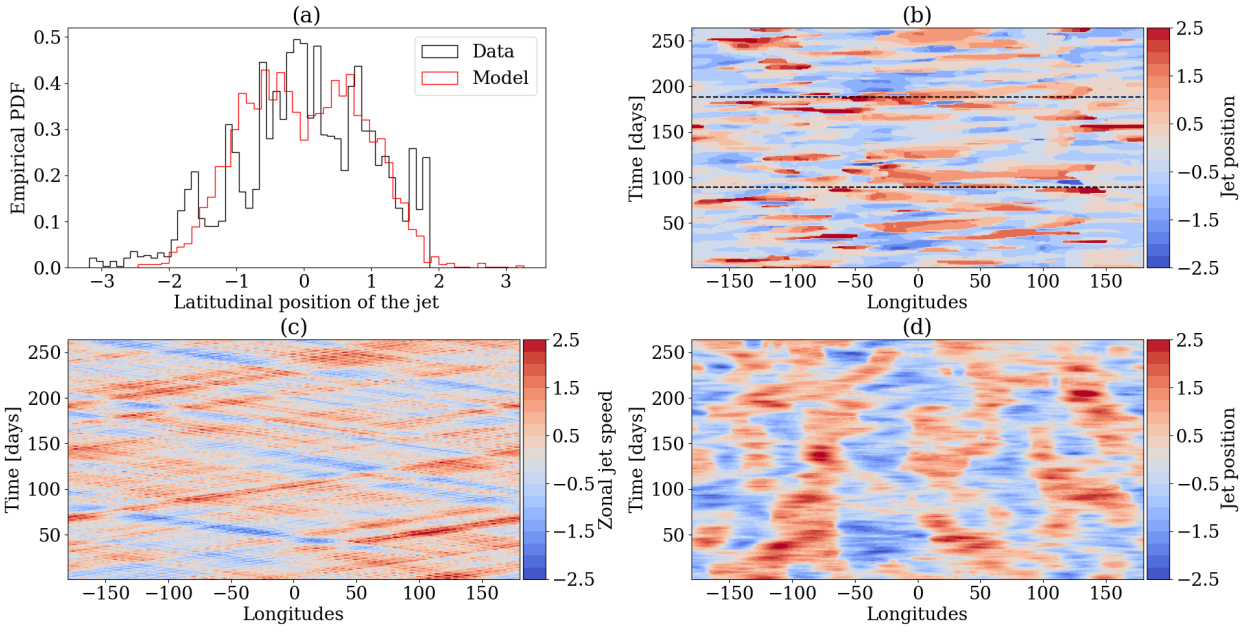

FIG. 21. **Perturbed spatial model for jet position.** (a) Histograms at lon=0° of jet latitudinal position for the data (black) and the model (red). (b) Hovmöller diagram of latitudinal jet position for the data over three winters (2000-2003). Horizontal dashed lines represent the limits between the three winters for the data, so that there is no continuity at those times. (c) Hovmöller diagram of zonal wind speed at the jet for the model over three winters and (d) corresponding Hovmöller diagram of latitudinal jet position for the model over three winters. The model is computed at a 0.01 day time step over 10 years but is plotted every 100 time steps (one day) to be comparable to the data.

Finally we present the "violin" plots of local dynamical metrics computed on the data and on the model in Figure 22. The violin plots display the distributions of local metrics in a manner similar to a vertical histogram. Comparing the local dimension d and local persistence θ^{-1} between the model and the reanalysis data allows us to ensure similarity between their dynamical properties. More precisely, on the first hand, d corresponds to the active number of degrees of freedom in the system and therefore a low value of d means that the coupled oscillators behave as a lower order system: they are partly synchronized (see Pons et al. (2020) for the link between a low local dimension and synchronization). On the other hand, θ^{-1} compares the time scale of the persistence between the different states, that is the mean time spend around each particular state in the phase space. As in Figure 5, both indicators are computed using only data over the Euro-Atlantic sector

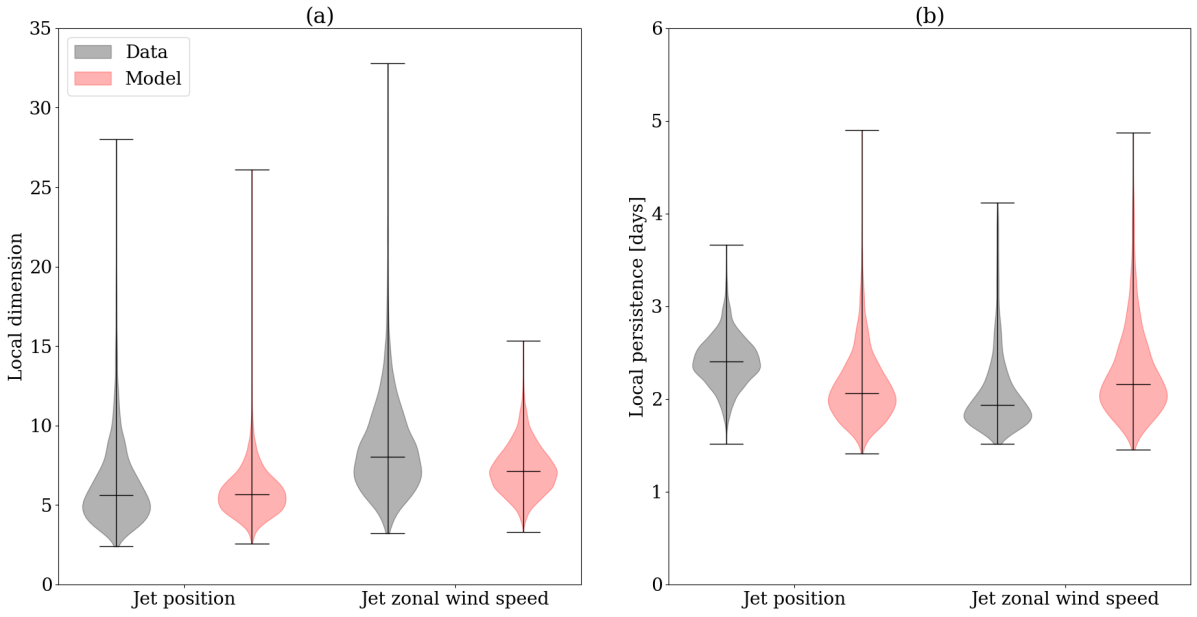

FIG. 22. **Local dynamical metrics: model and data.** Violin plots of (a) local dimension and (b) local persistence for the jet position (left) and jet zonal wind speed (right) for the data (grey) and the model (red). The model is computed at a 0.01 day time step over 10 years but local dynamical metrics are computed with the series of the model output taken every 100 time steps (one day) to be comparable to the data.

(45°W–45°E), and therefore 360 longitude grid points for the model, because the inferred dynamics is supposed to be valid only around this region.

For the results of the model to be comparable with the data, the local dynamical metrics are computed with a sample of the model output taken every 100 time steps (one day). For the model of zonal wind, we also apply a 4-day low-pass Lanczos filter to remove the effect of baroclinic instabilities represented here by the perturbation term S^i. The results are not sensitive to the cutoff period of the filter, as long as it is between 4 and 10 days. This is particularly important for local persistence as we explained previously. The distributions of local dimension and persistence, both in the jet position model and jet zonal wind speed model are similar to the one observed on the data, which comforts us in the dynamical relevance of our model.

5. Discussion

In the previous sections we investigated the behavior of a model of the eddy-driven jet. We have shown that the northward and southward excursions of the jet can be used as a diagnostic tool for blocking events. The latter occur on a time scale smaller than a day and are associated with a strong decrease of zonal wind speed on the jet 2–3 days prior to the excursion. By looking at Northern Hemisphere maps of the geopotential height and horizontal wind speeds, we have shown that those excursions are strongly linked to blocking-like events.

By investigating the recurrent dynamics of zonal wind speed at the jet, we proposed a non-linear and stochastically perturbed oscillator point model to represent it. The jet dynamics was then represented as a forced Langevin equation. Even though those 0D coupled stochastic models exhibit some of the characteristics of the behavior of zonal wind speed at the jet and jet position variability, they do not take into account the spatial variability and their temporal characteristics are not consistent with those observed on the jet.

We therefore proposed two stochastic coupled dynamical models. The first one is for the zonal wind speed on the jet based on the coupling between the oscillator previously identified, leading to the Toda lattice, and a stochastic but spatially meaningful disturbance, modeling in particular the spatial characteristics of Rossby wave breaking. The second one is for the latitudinal jet position based on coupled forced Langevin equations. The model for the zonal wind speed on the jet has the remarkable property of having temporal and spatial characteristics very close to the ERA5 data, especially with the temporal spectrum. It therefore naturally comes to mind to ask why this model seems suitable to represent the dynamics of zonal wind speed on the jet. The answer could lie in the following two points: (i) the Toda lattice can be shown to be a discretized version of the Korteweg-de Vries equation (Toda 1975), which is known to sustain solutions in the form of solitons, i.e. solitary waves that propagate without deformation ; (ii) blocking events, or large northward/southward excursions of the jet, can be linked to soliton-like structures in the atmosphere (Malguzzi and Malanotte-Rizzoli 1984). Therefore the series of peaks observed in the spectra presented previously (Fig. 20 panel (b)), and well reproduced by the model, could represent a train of soliton waves that propagate in both directions along the jet and that cause northward and southward shifts in the jet latitudinal position when the amplitude of the soliton is negative.

This interpretation is consistent with the Hovmöller diagrams presented above, for the data or for the model.

When analyzing the variability of the jet, we have shown that coupled forced Langevin equations represent reasonably well the variability behavior of the latitudinal position of the jet. To explain physical mechanisms, we conjecture that the oscillatory nature of zonal wind speed in our model does not come from a feedback such as those proposed by Barnes and Hartmann (2011) and Woollings et al. (2018b) between jet speed, jet variability and wave-mean flow interaction. The feedback mechanism, creating an oscillatory behavior is intrinsic of the model behavior via the recurrence function applied on u. This intrinsic oscillatory behavior may be related to the mechanism proposed by Ambaum and Novak (2014) to model storm track variability with a non-linear oscillator evolving in a potential well very similar to the one we proposed: the interaction between local baroclinicity and eddy heat flux. The physical law explaining the increasing variability of the jet position when its speed is low is however still not clear, even if it is strongly supported by either empirical (Woollings et al. 2018b) and numerical (Vallis et al. 2004) studies. Those are the reasons why a physics-informed stochastic model such as the one we proposed here is relevant and consistent with what has been proposed in the literature (e.g. Masato et al. 2009; Paradise et al. 2019).

Overall, we demonstrated that by mixing ideas of dynamical systems theory, especially embedding of climate data, and knowledge of the physical phenomena at stake, in particular the fact that the variability of the jet latitudinal position increases as the jet zonal wind speed decreases, we can propose reasonable coupled models of the eddy-driven jet stream latitudinal position and its zonal wind speed, representing in particular the northward and southward excursions events, therefore extending the model proposed by Faranda et al. (2019). The proposed model is obviously a very crude representation of the real jet and therefore our model has three main caveats. First, the model was build to represent blocking events in the Euro-Atlantic sector in winter, and the jet behavior could be different in other sectors and during other seasons, especially over land and at the western side of ocean basins as revealed by the blocked frequency at these locations (fig. 3). Second, the model does not include any geographical inhomogeneities, contrary to the real jet as seen in section 3. It is likely that such inhomogeneties could be taken into account in the model, for example by introducing constant forcing which would differ over land and over sea as in Faranda et al. (2019).

Last, the temporal and spatial spectrum of jet position and zonal wind speed do not perfectly fit the real data as shown previously, which reveals the presence of dynamical features that were not taken into account.

6. Conclusions

We investigated the variability of the northern eddy-driven jet stream latitudinal position and zonal wind speed with ERA5 reanalysis data over the period 1979–2019. We showed that northward and southward shifts of the jet latitudinal position are preceded by a strong decrease in jet zonal wind speed 2-3 days before the excursion, which is not the case for zonal wind speed at a fixed latitude, e.g. at 45°N. We also showed that the dynamics of the jet zonal wind speed can be represented by a non-linear randomly perturbed oscillator.

Those two results are used to construct a point stochastic model of jet latitudinal position and jet zonal wind speed, which is then extended to all longitudes using two coupled non-linear lattices modelling those two variables. The jet zonal wind speed is modelled as a perturbed Toda lattice, whereas the jet latitudinal position is modelled as coupled forced Langevin equations. Those coupled models compare surprisingly good to empirical data when it comes to their temporal and spatial characteristics, and are therefore able to grasp the main features of the jet behavior during the onset and the decay of blocking events. We also proposed that the success of the Toda lattice to model the propagation of disturbances along the jet can be a result of the capacity of this lattice to propagate solitons, which could themselves be related to blocking events. In the end, we extended the minimal dynamical model proposed by Faranda et al. (2019), which strengthens their conclusion regarding the possibility of reducing complex mid-latitude circulation dynamics to low-dimensional representations given by conceptual models.

The results are consistent with previous results available in the literature, either on the link between jet variability and jet wind speed (Woollings et al. 2018b), or the use of non-linear oscillators to represent storm track variability (Ambaum and Novak 2014). Future analysis could investigate whether a similar model can be made in the Southern hemisphere, where the role of topography is much less important. It could also be relevant to investigate how this model can be used in a context of global warming, i.e. the sensitivity of key parameters to the reduction of the tropical–polar temperature gradient (Petoukhov et al. 2013). Intense research has indeed

been carried out to better understand how the dynamics of the jet will change with climate change (Woollings et al. 2018a), especially in relation with Arctic amplification and the decrease of the meridional temperature gradient.

The performance of coupled climate models to represent blocking statistics has been deemed to be low (Davini and d'Andrea 2020). We hence do believe that our simple models of the jet behavior, can help improve the next generation of climate models in representing key atmospheric features in the midlatitudes.

Acknowledgments. This work was part of RN's Master's thesis at the University Paris-Sorbonne (Master MOCIS). We thank Francis Codron, Gabriele Messori, Sandro Vaienti and Vladimir Zeitlin for their comments on the behavior of the jet stream and the use of simplified dynamical systems to model it. This work was funded by French ANR project No. ANR-20-CE01-0008 (SAMPRACE), the ANR-19-ERC7-0003 project (BOREAS) and the LEFE-MANU (DYNCLIC) CRNS grant.

Data availability statement. The ERA5 data are available on the Copernicus web site (https://cds.climate.copernicus.eu/cdsapp!/home). The results of the detection of the jet position are available on demand.

References

Ambaum, M. H., and L. Novak, 2014: A nonlinear oscillator describing storm track variability. *Quarterly Journal of the Royal Meteorological Society*, **140 (685)**, 2680–2684.

Attinger, R., J. H. Keller, M. Köhler, J. Riboldi, and C. M. Grams, 2019: Representation of atmospheric blocking in the new global non-hydrostatic weather prediction model icon. *Meteorologische Zeitschrift*, **28 (5)**, 429–446.

Barnes, E. A., and D. L. Hartmann, 2011: Rossby wave scales, propagation, and the variability of eddy-driven jets. *Journal of the atmospheric sciences*, **68 (12)**, 2893–2908.

Barriopedro, D., R. García-Herrera, A. R. Lupo, and E. Hernández, 2006: A climatology of northern hemisphere blocking. *Journal of Climate*, **19 (6)**, 1042–1063.

Barriopedro, D., R. García-Herrera, and R. M. Trigo, 2010: Application of blocking diagnosis methods to general circulation models. part i: A novel detection scheme. *Climate dynamics*, **35 (7)**, 1373–1391.

Charney, J. G., 1947: The dynamics of long waves in a baroclinic westerly current. *Journal of Atmospheric Sciences*, **4 (5)**, 136–162.

Charney, J. G., and J. G. DeVore, 1979: Multiple flow equilibria in the atmosphere and blocking. *Journal of Atmospheric Sciences*, **36 (7)**, 1205–1216.

Davini, P., and F. D'Andrea, 2016: Northern hemisphere atmospheric blocking representation in global climate models: Twenty years of improvements? *Journal of Climate*, **29 (24)**, 8823–8840.

Davini, P., and F. d'Andrea, 2020: From cmip3 to cmip6: Northern hemisphere atmospheric blocking simulation in present and future climate. *Journal of Climate*, **33 (23)**, 10 021–10 038.

Dijkstra, H. A., 2016: Understanding climate variability using dynamical systems theory. *The Fluid Dynamics of Climate*, Springer, 1–38.

Dole, R., and Coauthors, 2011: Was there a basis for anticipating the 2010 russian heat wave? *Geophysical Research Letters*, **38 (6)**.

Duchon, C. E., 1979: Lanczos filtering in one and two dimensions. *Journal of Applied Meteorology and Climatology*, **18 (8)**, 1016–1022.

Faranda, D., G. Masato, N. Moloney, Y. Sato, F. Daviaud, B. Dubrulle, and P. Yiou, 2016: The switching between zonal and blocked mid-latitude atmospheric circulation: a dynamical system perspective. *Climate Dynamics*, **47 (5)**, 1587–1599.

Faranda, D., G. Messori, and P. Yiou, 2017: Dynamical proxies of north atlantic predictability and extremes. *Scientific reports*, **7 (1)**, 1–10.

Faranda, D., Y. Sato, G. Messori, N. R. Moloney, and P. Yiou, 2019: Minimal dynamical systems model of the northern hemisphere jet stream via embedding of climate data. *Earth System Dynamics*, **10 (3)**, 555–567.

Frederiksen, J., 1982: A unified three-dimensional instability theory of the onset of blocking and cyclogenesis. *Journal of Atmospheric Sciences*, **39 (5)**, 969–982.

Ghil, M., 1987: Dynamics, statistics and predictability of planetary flow regimes. *Irreversible Phenomena and Dynamical Systems Analysis in Geosciences*, Springer, 241–283.

Ghil, M., M. D. Chekroun, and E. Simonnet, 2008: Climate dynamics and fluid mechanics: Natural variability and related uncertainties. *Physica D: Nonlinear Phenomena*, **237 (14-17)**, 2111–2126.

Ghil, M., and V. Lucarini, 2020: The physics of climate variability and climate change. *Reviews of Modern Physics*, **92 (3)**, 035 002.

Haines, K., and P. Malanotte-Rizzoli, 1991: Isolated anomalies in westerly jet streams: A unified approach. *Journal of Atmospheric Sciences*, **48 (4)**, 510–526.

748 Hansen, A. R., 1986: Observational characteristics of atmospheric planetary waves with bimodal
749 amplitude distributions. *Advances in Geophysics*, Vol. 29, Elsevier, 101–133.

750 Held, I. M., 1975: Momentum transport by quasi-geostrophic eddies. *J. Atmos. Sci*, **32 (7)**, 1494–
751 1497.

752 Held, I. M., and A. Y. Hou, 1980: Nonlinear axially symmetric circulations in a nearly inviscid
753 atmosphere. *Journal of the Atmospheric Sciences*, **37 (3)**, 515–533.

754 Hersbach, H., and Coauthors, 2020: The era5 global reanalysis. *Quarterly Journal of the Royal*
755 *Meteorological Society*, **146 (730)**, 1999–2049.

756 Holton, J. R., 1973: An introduction to dynamic meteorology. *American Journal of Physics*, **41 (5)**,
757 752–754.

758 Hoskins, B. J., and I. N. James, 2014: *Fluid dynamics of the mid-latitude atmosphere*. John Wiley
759 & Sons.

760 Huang, C. S., and N. Nakamura, 2016: Local finite-amplitude wave activity as a diagnostic of
761 anomalous weather events. *Journal of the Atmospheric Sciences*, **73 (1)**, 211–229.

762 Hurrell, J. W., and C. Deser, 2010: North atlantic climate variability: the role of the north atlantic
763 oscillation. *Journal of marine systems*, **79 (3-4)**, 231–244.

764 Kalnay-Rivas, E., and L.-O. Merkine, 1981: A simple mechanism for blocking. *Journal of Atmo-*
765 *spheric Sciences*, **38 (10)**, 2077–2091.

766 Kautz, L.-A., O. Martius, S. Pfahl, J. G. Pinto, A. M. Ramos, P. M. Sousa, and T. Woollings, 2021:
767 Atmospheric blocking and weather extremes over the euro-atlantic sector–a review. *Weather and*
768 *Climate Dynamics Discussions*, 1–43.

769 Koch, P., H. Wernli, and H. C. Davies, 2006: An event-based jet-stream climatology and typology.
770 *International Journal of Climatology: A Journal of the Royal Meteorological Society*, **26 (3)**,
771 283–301.

772 Lee, S., and H.-k. Kim, 2003: The dynamical relationship between subtropical and eddy-driven
773 jets. *Journal of the atmospheric sciences*, **60 (12)**, 1490–1503.

Legras, B., and M. Ghil, 1985: Persistent anomalies, blocking and variations in atmospheric predictability. *Journal of Atmospheric Sciences*, **42 (5)**, 433–471.

Lucarini, V., and Coauthors, 2016: *Extremes and recurrence in dynamical systems*. John Wiley & Sons.

Lupo, A. R., 2020: Atmospheric blocking events: a review. *Annals of the New York Academy of Sciences*.

Malguzzi, P., and P. Malanotte-Rizzoli, 1984: Nonlinear stationary rossby waves on nonuniform zonal winds and atmospheric blocking. part i: The analytical theory. *Journal of Atmospheric Sciences*, **41 (17)**, 2620–2628.

Mann, M. E., S. Rahmstorf, K. Kornhuber, B. A. Steinman, S. K. Miller, S. Petri, and D. Coumou, 2018: Projected changes in persistent extreme summer weather events: The role of quasi-resonant amplification. *Science advances*, **4 (10)**, eaat3272.

Masato, G., B. J. Hoskins, and T. Woollings, 2013: Wave-breaking characteristics of northern hemisphere winter blocking: A two-dimensional approach. *Journal of Climate*, **26 (13)**, 4535–4549.

Masato, G., B. J. Hoskins, and T. J. Woollings, 2009: Can the frequency of blocking be described by a red noise process? *Journal of the atmospheric sciences*, **66 (7)**, 2143–2149.

McWilliams, J. C., G. R. Flierl, V. D. Larichev, and G. M. Reznik, 1981: Numerical studies of barotropic modons. *Dynamics of Atmospheres and Oceans*, **5 (4)**, 219–238.

Messori, G., N. Harnik, E. Madonna, O. Lachmy, and D. Faranda, 2021: A dynamical systems characterization of atmospheric jet regimes. *Earth System Dynamics*, **12 (1)**, 233–251.

Moloney, N. R., D. Faranda, and Y. Sato, 2019: An overview of the extremal index. *Chaos: An Interdisciplinary Journal of Nonlinear Science*, **29 (2)**, 022 101.

Nakamura, N., and C. S. Huang, 2018: Atmospheric blocking as a traffic jam in the jet stream. *Science*, **361 (6397)**, 42–47.

Paradise, A., C. B. Rocha, P. Barpanda, and N. Nakamura, 2019: Blocking statistics in a varying climate: Lessons from a "traffic jam" model with pseudostochastic forcing. *Journal of the Atmospheric Sciences*, **76 (10)**, 3013–3027.

Pelly, J. L., and B. J. Hoskins, 2003: A new perspective on blocking. *Journal of the atmospheric sciences*, **60 (5)**, 743–755.

Petoukhov, V., S. Rahmstorf, S. Petri, and H. J. Schellnhuber, 2013: Quasiresonant amplification of planetary waves and recent northern hemisphere weather extremes. *Proceedings of the National Academy of Sciences*, **110 (14)**, 5336–5341.

Pons, F. M. E., G. Messori, M. C. Alvarez-Castro, and D. Faranda, 2020: Sampling hyperspheres via extreme value theory: implications for measuring attractor dimensions. *Journal of statistical physics*, **179 (5)**, 1698–1717.

Rex, D. F., 1950: Blocking action in the middle troposphere and its effect upon regional climate. *Tellus*, **2 (4)**, 275–301.

Rhines, P. B., 1975: Waves and turbulence on a beta-plane. *Journal of Fluid Mechanics*, **69 (3)**, 417–443.

Röthlisberger, M., S. Pfahl, and O. Martius, 2016: Regional-scale jet waviness modulates the occurrence of midlatitude weather extremes. *Geophysical Research Letters*, **43 (20)**, 10–989.

Scherrer, S. C., M. Croci-Maspoli, C. Schwierz, and C. Appenzeller, 2006: Two-dimensional indices of atmospheric blocking and their statistical relationship with winter climate patterns in the euro-atlantic region. *International Journal of Climatology: A Journal of the Royal Meteorological Society*, **26 (2)**, 233–249.

Schwierz, C., M. Croci-Maspoli, and H. Davies, 2004: Perspicacious indicators of atmospheric blocking. *Geophysical research letters*, **31 (6)**.

Simmons, A., J. Wallace, and G. Branstator, 1983: Barotropic wave propagation and instability, and atmospheric teleconnection patterns. *Journal of Atmospheric Sciences*, **40 (6)**, 1363–1392.

Süveges, M., 2007: Likelihood estimation of the extremal index. *Extremes*, **10 (1-2)**, 41–55.

Tibaldi, S., and F. Molteni, 1990: On the operational predictability of blocking. *Tellus A*, **42 (3)**, 343–365.

Toda, M., 1967: Vibration of a chain with nonlinear interaction. *Journal of the Physical Society of Japan*, **22 (2)**, 431–436.

Toda, M., 1975: Studies of a non-linear lattice. *Physics Reports*, **18 (1)**, 1–123.

Tung, K., and R. Lindzen, 1979: A theory of stationary long waves. part i: A simple theory of blocking. *Monthly Weather Review*, **107 (6)**, 714–734.

Tyrlis, E., and B. Hoskins, 2008: Aspects of a northern hemisphere atmospheric blocking climatology. *Journal of the Atmospheric Sciences*, **65 (5)**, 1638–1652.

Vallis, G. K., E. P. Gerber, P. J. Kushner, and B. A. Cash, 2004: A mechanism and simple dynamical model of the north atlantic oscillation and annular modes. *Journal of the atmospheric sciences*, **61 (3)**, 264–280.

Vautard, R., 1990: Multiple weather regimes over the north atlantic: Analysis of precursors and successors. *Monthly weather review*, **118 (10)**, 2056–2081.

Woollings, T., A. Hannachi, and B. Hoskins, 2010: Variability of the north atlantic eddy-driven jet stream. *Quarterly Journal of the Royal Meteorological Society*, **136 (649)**, 856–868.

Woollings, T., and Coauthors, 2018a: Blocking and its response to climate change. *Current climate change reports*, **4 (3)**, 287–300.

Woollings, T., and Coauthors, 2018b: Daily to decadal modulation of jet variability. *Journal of Climate*, **31 (4)**, 1297–1314.